JGR Earth Surface

RESEARCH ARTICLE
10.1029/2022JF006986

Shaping the Huara Intrusive Complex in the Hyperarid Atacama Desert—Erosional Near-Stasis Contrasting High Topographic Gradients

Benedikt Ritter[1], Joel Mohren[1], Steven A. Binnie[1], Volker Wennrich[1], István Dunkl[2], Richard Albert[3], Axel Gerdes[3], Sandro LoBue[1], and Tibor J. Dunai[1]

[1]Institute of Geology & Mineralogy, University of Cologne, Cologne, Germany, [2]Sedimentology and Environmental Geology, Geoscience Centre, Georg-August Universität Göttingen, Göttingen, Germany, [3]Frankfurt Isotope and Element Research Center (FIERCE), Department of Geoscience, Goethe University Frankfurt, Frankfurt, Germany

Key Points:

- Extremely low basin erosion rates (<1 m/Myr) in the hyperarid Atacama prevailed since the Pliocene, contrasting high relief topography
- Higher bedrock erosion rates indicate that the tectonic activity is the active landscape forming mechanism
- The capacity to erode is reduced by the effects of atmospheric deposition, soil inflation, and channel boulder accumulations

Supporting Information:

Supporting Information may be found in the online version of this article.

Correspondence to:

B. Ritter,
benedikt.ritter@uni-koeln.de

Citation:

Ritter, B., Mohren, J., Binnie, S. A., Wennrich, V., Dunkl, I., Albert, R., et al. (2023). Shaping the Huara Intrusive Complex in the hyperarid Atacama Desert—Erosional near-stasis contrasting high topographic gradients. *Journal of Geophysical Research: Earth Surface*, *128*, e2022JF006986. https://doi.org/10.1029/2022JF006986

Received 27 OCT 2022
Accepted 28 FEB 2023
Corrected 14 APR 2023

This article was corrected on 14 APR 2023. See the end of the full text for details.

Author Contributions:

Conceptualization: Benedikt Ritter
Data curation: Benedikt Ritter
Formal analysis: Benedikt Ritter, Joel Mohren, István Dunkl, Richard Albert, Axel Gerdes, Sandro LoBue, Tibor J. Dunai
Funding acquisition: Tibor J. Dunai

Abstract The Atacama Desert is one of the driest and oldest deserts on Earth, with extremely low precipitation rates (<2 mm/yr). Mostly abiotic hyperarid environmental conditions prevail, and surface processes act at extremely low rates over the long-term. To gain knowledge about the rate of surface processes and age of landscapes in desert environments, terrestrial cosmogenic nuclide derived erosion rate estimates can be used. Within the Huara Intrusive Complex, situated in the hyperarid core of the Atacama Desert, basin-averaged bedrock erosion rates from channel sediments are extremely low, that is, less than 1 m/Myr. Such low rates indicate that fluvial processes operate very slowly or are almost absent. Bedrock erosion rates of channel knickpoints, however, reveal one to two orders of magnitude higher erosion rates (2–12 m/Myr). Erosion rates are remarkably low when compared to the steep surrounding topography. Tectonic uplift creates higher gravitational potentials for surface processes, controlling the overall erosion rate capacity. However, erosion itself is taking place by local precipitation capable of exceeding thresholds for surface activity. In the Atacama Desert, this happens only due to rare severe precipitation events, explaining the extremely low erosion rates. The efficiency of these events is modulated by local intrinsic processes and conditions, such as high infiltration capacities of Atacama soils and/or large channel boulder accumulations. Due to the virtual absence of these precipitation events capable of erosion, the landscape appears to be in hibernation.

Plain Language Summary The Atacama Desert is one of the driest and oldest deserts on Earth, with extremely low precipitation rates (<2 mm/yr). Surface processes operate at very low rates and on small spatial scales. To understand the rates of surface activity, cosmogenic nuclides are a widely used tool to constrain the exposure duration of sediments on the Earth's surface. Within the Huara Intrusive Complex, situated in the hyperarid core of the Atacama, basin-averaged erosion rates from channel sediments are extremely low. Such low rates indicate that the transport of sediment is very slow or almost absent, revealing a landscape in hibernation. Bedrock erosion rates in channels, however, are one to two orders higher. The studied catchments have been subject to Quaternary tectonic activity, which can explain higher bedrock erosion rates. Rare precipitation events, typical for desert environments, have to be strong enough to provoke erosion. Processes associated with extreme long-term aridity modulate the erosive impact of precipitation events; for example, $CaSO_4$-rich soils soak up water preventing surface runoff or channel boulder accumulations buffer surface flow reducing the capacity to erode.

1. Introduction

Processes governing fluvial topography formation in hyperarid abiotic environments are generally limited to low rates over the long term and are predominantly controlled by rare but intense precipitation events (e.g., Aguilar et al., 2020; Jordan et al., 2015; Shmilovitz et al., 2020). The Atacama Desert of northern Chile is no exception and yields erosion rates that are among the lowest measured on Earth (basin averaged erosion rates ~0.5–40 m/Myr, Kober et al., 2007; Mohren et al., 2020; C. Placzek et al., 2014; C. J. Placzek et al., 2010; Starke et al., 2017). Quantitative assessments of such rates in these extremely arid to hyperarid environments remain difficult due to the rarity of surface activity. Hence, the application of proxies and/or tools, which integrate over timescales of up to hundreds of thousands of years, is required. In the hyperarid Atacama Desert, such timescales have been shown to be captured by the analysis of terrestrial cosmogenic nuclides (TCNs) (S. Binnie et al., 2020;

Investigation: Benedikt Ritter, Tibor J. Dunai
Methodology: Benedikt Ritter, Joel Mohren, Steven A. Binnie, Volker Wennrich, István Dunkl, Richard Albert, Axel Gerdes, Sandro LoBue, Tibor J. Dunai
Project Administration: Benedikt Ritter
Software: Benedikt Ritter, Joel Mohren
Supervision: Tibor J. Dunai
Validation: Benedikt Ritter, Joel Mohren, Steven A. Binnie
Visualization: Benedikt Ritter
Writing – original draft: Benedikt Ritter, Joel Mohren
Writing – review & editing: Benedikt Ritter, Joel Mohren, Steven A. Binnie, Volker Wennrich, István Dunkl, Richard Albert, Axel Gerdes, Sandro LoBue, Tibor J. Dunai

Dunai et al., 2005; Evenstar et al., 2017; Kober et al., 2007; Mohren et al., 2020; C. Placzek et al., 2014; C. J. Placzek et al., 2010; Ritter et al., 2018; Starke et al., 2017). From these studies, it becomes evident that despite long-term aridity, erosional processes operate at different spatial and temporal scales and that they vary depending on the sampled geomorphological feature (Kober et al., 2007; Matmon et al., 2015; Mohren et al., 2020; C. Placzek et al., 2014; C. J. Placzek et al., 2010; Starke et al., 2017). These findings have to be reconciled with the preservation of large tracts of relict landscapes in the "hyperarid core" of the Atacama Desert (predominantly spanning the Coastal Cordillera, from 19° to 22°S, Ritter et al., 2018) that indicate the general inactivity of major landscape-forming processes, such as the shedding of large volumes of sediments and deep incisions.

Catchments situated in the Coastal Cordillera, disconnected from Andean sourced discharge (Figure 1), allow us to investigate surface processes and rates under predominantly extreme and long-term hyperarid conditions. In these abiotic environments, drainage basins can be regarded as natural laboratories to investigate the influence of rare, but intense, precipitation events on topography formation over time. Persistent aridity means that the gross topographic form is a function of large-scale tectonic structures (Allmendinger & González, 2010; S. Binnie et al., 2020; Ritter et al., 2018). Moreover, due to the scarcity of precipitation, other processes may be at play controlling and/or modulating surface activity, such as: (a) widespread accumulation of a landscape draping $CaSO_4$-rich soil that has accumulated by atmospheric deposition and appears to prevent surface runoff by increasing the infiltration capacity of soils (Jordan et al., 2015; May et al., 2020); (b) armoring by large boulder accumulations within incised channels, reducing torrential precipitation induced erosion (Fang et al., 2017; Yager et al., 2007); or (c) slope stabilization due to subsurface salt incrustation, suppressing sediment detachment/release (Mohren et al., 2020).

In this study, we investigate the interactions of tectonic activity, hyperaridity, and soil inflation on fluvial erosion in an extreme hyperarid and high relief environment. We measured ^{26}Al and ^{10}Be cosmogenic nuclide concentrations from channel sediments and bedrock within the Huara Intrusive Complex (HIC) to calculate apparent basin-averaged and bedrock outcrop erosion rates. High-resolution satellite imagery (Pléiades-1B) and a digital terrain model (DTM) were used to calculate catchment metrics and map geomorphological features. Moreover, we dated outcropping tephra deposits to constrain erosion in our catchments independently of the cosmogenic methodology, allowing us to consider biases in the cosmogenic nuclide approach.

2. Regional Setting

2.1. Geological and Geomorphological Background

The study area is located in the Coastal Cordillera of the northern Atacama Desert (Figure 1). The Coastal Cordillera reaches elevations between 900 and 1,700 m a.s.l. and spans between the coastal cliff and Pacific Ocean to the west and the Central Depression to the east. Being spatially isolated from other larger sedimentation systems, the Coastal Cordillera between 19° and 23°S experienced the evolution of aridity without being significantly influenced by allochthonous climate signals, as is the case for landscapes in the Central Depression. Several studies have already indicated that predominantly arid to hyperarid conditions in this part of the Atacama Desert have prevailed at least since the Early Miocene (Dunai et al., 2005; Evenstar et al., 2017; Ritter et al., 2018, 2022). Reasons for this persistent aridity are manifold. Important factors are as follows: (a) its geographic position within the range of the subtropical high pressure belt (Houston, 2006); (b) upwelling of the cold Humboldt current in conjunction with the long-term persistence of an atmospheric inversion layer hampering the uptake of Pacific moisture, and trapping it below 1,000 m a.s.l (e.g., Garreaud et al., 2009, 2010); (c) the orogenic rain shadow effect of the Andes to the east (e.g., Garreaud et al., 2009, 2010; Houston, 2006; Houston & Hartley, 2003), as well as (d) a continental rain shadow effect for moisture originating from the Atlantic before moving over the South American continent toward the Atacama Desert (Houston, 2006).

2.2. Study Site—Huara Intrusive Complex

The study site is located in the Pampa de la Perdiz in the eastern part of the Coastal Cordillera, approximately 30 km NE of Iquique (Figure 2). This study focusses on small (<7 km^2) catchments draining the Huara Intrusive Complex (HIC). The granodioritic HIC (~140–136 Ma, Vásquez & Sepúlveda, 2013) covering an area of ~140 km^2 marks the eastern border to the Central Depression and forms a topographic high of up to ~1,700 m a.s.l. (surrounding area at an elevation of ~1,000–1,200 m a.s.l.). Previous cosmogenic exposure dating of alluvial fan

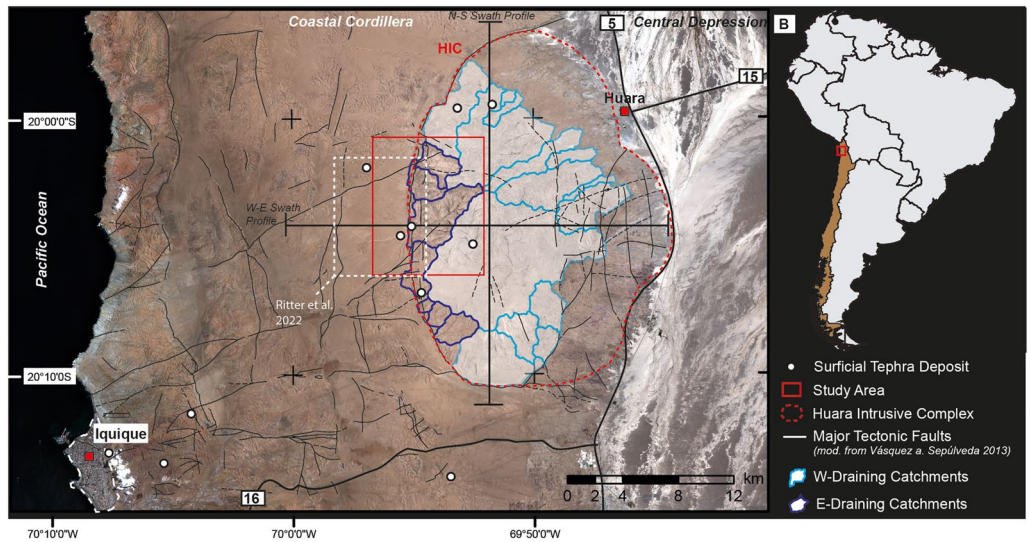

Figure 1. Sentinel true-color image showing the study area located approximately 30 km northeast of Iquique within the Coastal Cordillera (created using ArcGIS Pro 2.8.1—pro.arcgis.com—and Adobe Illustrator 2022—adobe.com). Major tectonic fault systems are indicated in black from Vásquez and Sepúlveda (2013) and complemented by own mapping (this study). The surficial extension of the Huara Intrusive Complex (HIC) is indicated with dashed red lines. Dark blue (westward directed) and light blue (eastward draining) colors encircle major catchments within the HIC. The red rectangle highlights the study area and the white rectangle marks the study area of Ritter et al. (2022). Straight black lines indicate swath profiles, shown in Figure S1 in Supporting Information S1.

surfaces to the west of the HIC (Figure 2) indicates that the overall fluvial geomorphology was presumably set during the Oligocene and Early Miocene and that large-scale deposition of erosional products essentially ceased during the Early Miocene (Ritter et al., 2022).

Western boundary faults caused uplift and eastward tilting of the HIC (Figure 2, swath profiles Figure S1 in Supporting Information S1). The western escarpment of the HIC is delimited by two tectonic faults, along which calcareous sandstones from the Caleta Lígate Formation are exposed (Late Jurassic/Early Cretaceous, Vásquez & Sepúlveda, 2013). Tectonic damming of small basins was initiated by the uplift of the westernmost reverse fault, causing the formation of basins alternating between endorheic and temporally partly exorheic conditions since approximately ~5 Ma (Ritter et al., 2022). Fully endorheic conditions prevailed presumably since 600–700 ka (Ritter et al., 2022). Local mean annual precipitation rates as recently measured by Hoffmeister (2018), at the CRC1211 #23 weather station, are less than 6.52 mm/yr (including heavy fog) during the measuring period March 2018–July 2020 (for location see Figure 2). We assume that precipitation rates are similar across the study area, although higher precipitation due to a local orographic effect of the higher elevated catchments cannot be excluded with certainty. This study focusses on three catchments that all currently terminate in endorheic clay pans and cover similar relief but differ in size and consequently in topographic gradients. These catchments are presented in the following.

The southern catchment (SC, ~6.4 km^2) extends about 6 km into the HIC in the N-E direction. The longitudinal channel profile is almost linear to weakly convex upward, with several weakly developed knickpoints (Figure 2). The hillslopes within this catchment are largely covered by debris originating from local bedrock outcrops uphill (Figures 3a and 3b). Some slopes show "zebra stripe" pattern (Owen et al., 2013), that is, "*surface clasts organized into distinct, contour-parallel bands separated by bare soil*" (Figure 3e, Owen et al., 2013); however, the majority of larger boulders and gravels have accumulated in rills and channels (Figure 3f). Hillslopes in the downstream part of the catchment (i.e., below the lowest knickpoint) downstream are steep (20.9° ± 7.9°). The upstream area, above the lowest knickpoint, widens up to a U-shaped valley and hillslopes become gentler (15.8° ± 8.5°). The main channel in the upper catchment, and most of its tributaries are filled with boulders (Figure 4). The topography in the upper catchment is smooth with a cover of a $CaSO_4$-rich soils and slope debris (Figures 3a and 3b). In the lower part of the upper catchment, the main channel cuts a pristine (i.e., not reworked; pure and devoid of fluvial debris) near-surface tephra (Figure 4).

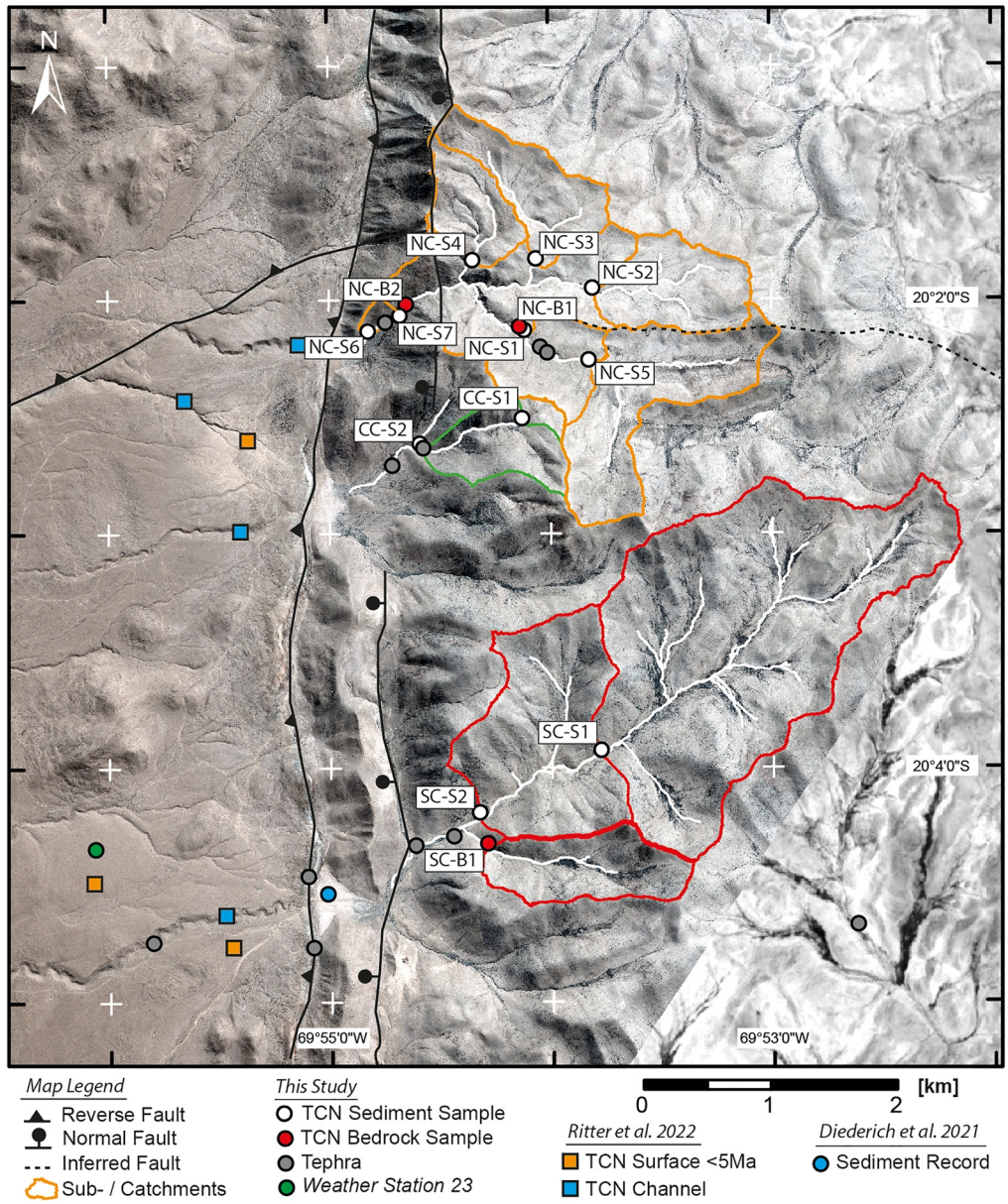

Figure 2. Overview map of the study area based on Pléiades 1B and Sentinel satellite imagery (created using ArcGIS Pro 2.8.1—pro.arcgis.com—and Adobe Illustrator 2022—adobe.com). Catchments of interest are outlined with colors (Northern in orange, Central in green, and Southern in red). Terrestrial cosmogenic nuclide (TCN) and tephra sampling sites are marked as well as TCN sampling sites (blue and orange squares) of Ritter et al. (2022) and Diederich et al. (2020). White lines represent channel networks of the studied catchments. Black lines represent fault scarps mapped by Vásquez and Sepúlveda (2013). Note that the adjacent Pampa de Perdiz is separated from the Huara Intrusive Complex (HIC) by two N-S running tectonic faults. Tectonic activity caused truncation of former catchments and the formation of endorheic basins. The morphology of the HIC is characterized by fluvial incision and greater relief than the adjacent pampas.

About ~2 km further to the north, a smaller catchment (central catchment [CC], ~0.7 km^2) extends up to ~1.5 km into the HIC, likewise in the N-E direction (Figure 2). The main channel and hillslopes are much steeper compared to the SC (Figure 5). The longitudinal channel profile is nearly linear to weakly convex upward with two knickpoints. The lowest part of the catchment and the terminal clay pan are largely covered by coarse alluvium, including large boulder fields, without an obvious permanent channel. Upstream of the depositional area, the confined channel is bound by contrasting hillslopes. Bedrock outcrops dominate the northern steep flanks (24.2° ± 9.1°), whereas the southern hillslopes are less steep (22.3° ± 7.6°) and smoother, covered by debris and $CaSO_4$-rich soils (Figures 3a and 3b). Upstream of the lowest knickpoint, the catchment widens, similar to the

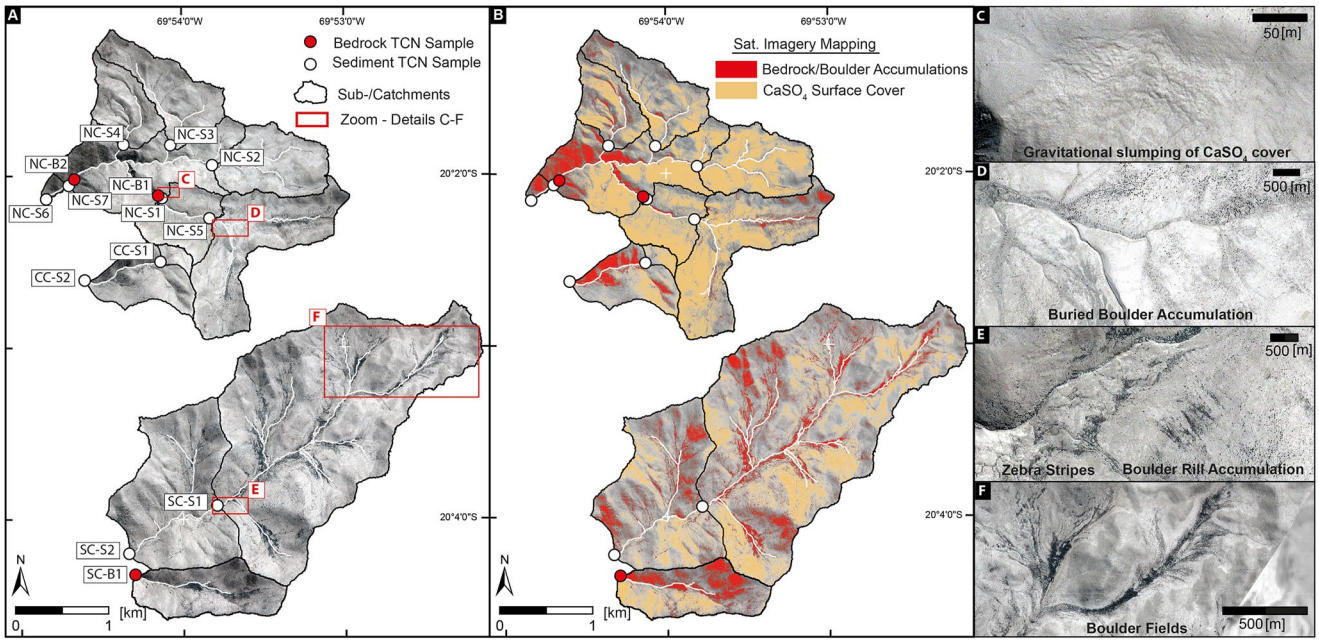

Figure 3. (a) Upstream catchments of the terrestrial cosmogenic nuclide sample sites based on pansharpened Pléiades 1B imagery (created using ArcGIS Pro 2.8.1—pro.arcgis.com—and Adobe Illustrator 2022—adobe.com). Red rectangles indicate examples of major surface processes within those catchments, see (c–f). (b) Mapping of surface deposits and outcropping bedrock was established using multispectral imagery (Pléiades 1B) to differentiate between surfaces dominated by either $CaSO_4$ cover (light brown) or bedrock /boulder accumulations (red). Note that within the northern catchment (NC) at higher elevations, $CaSO_4$ cover is prevalent, whereas the lower parts with steeper hillslopes are characterized by bedrock outcrops. For the southern catchment (SC), a dominance of boulder accumulations within the major channel network and an increasing cover of $CaSO_4$ in the upper parts of the catchment is indicated. (c) Gravitational slumping of $CaSO_4$-dominated hillslope surface in the NC. (d) Smaller boulder accumulations within the NC, which are partly buried. (e) Signs of zebra-stripe formation and boulders accumulating in rills on hillslopes within the SC. (f) Large boulder accumulations/fields filling up the entire channel system within the SC.

SC. Boulders have accumulated within the main channel and tributaries. Portions of the channel and adjacent hillslopes are covered with tephra.

The northern catchment (NC, ~4.9 km^2, ~1 km from CC) consists of one major channel in the lower reaches, which splits into several branches in the elevated part (Figure 2). The longitudinal channel profile is convex upwards with two prominent knickpoints. There is a stark contrast in the catchment morphology, as its lower part includes steep hillslopes and a steep channel profile, which opens up into a plateau-like, fluvially shaped landscape (Figure 5). In the transition zone, bedrock is outcropping within the channel, forming distinct bedrock knickpoints (Figures 4a and 4b). Below the transition zone, close to the endorheic pan, the main channel is largely filled up with debris, presumably directly sourced from the adjacent steep hillslopes. Locally, a gully has incised up to 2 m into the unconsolidated sediments filling the thalweg. The former flat-floored valley with the sediment-choked channel changes into a V-shaped valley and bedrock outcrops become more abundant, along with steeper hillslopes entering the transition zone further upstream. Bedrock outcrops dominate the northern hillslope and parts of the southern hillslopes in the transition zone (Figures 3a and 3b). Further upstream of the transition zone, the steep topography changes toward a more gently shaped fluvial morphology and a plateau-like, low relief landscape. Fields of large boulders and boulder-filled channels appear less developed as compared to the SCs and/or are buried by finer sediments (Figure 3d). Fluvial erosion in these catchments has formed a flat-bottom topography with low channel gradients (Figure 4j). Hillslopes and peaks are subdued and reveal no bedrock outcrops. Surfaces are widely covered by debris and concealed by a significant layer of $CaSO_4$ (Figures 3a and 3b). Mass movements on $CaSO_4$-mantled steep slopes are visible from satellite imagery (Figure 3c), possibly caused by oversteepening of slopes and potentially triggered by earthquakes. Smaller tributaries and hillslope rills are filled up with gravels and boulders, but to a much lesser extent compared to the SC. Fluvial erosion in this more elevated part of the NC appears to be minimal, and a more depositional character dominates the geomorphology than that observed further south. No major tephra accumulations were observed; however, minor tephra deposits are visible on eroding hillslopes and locally in incised channel banks (Figure 4).

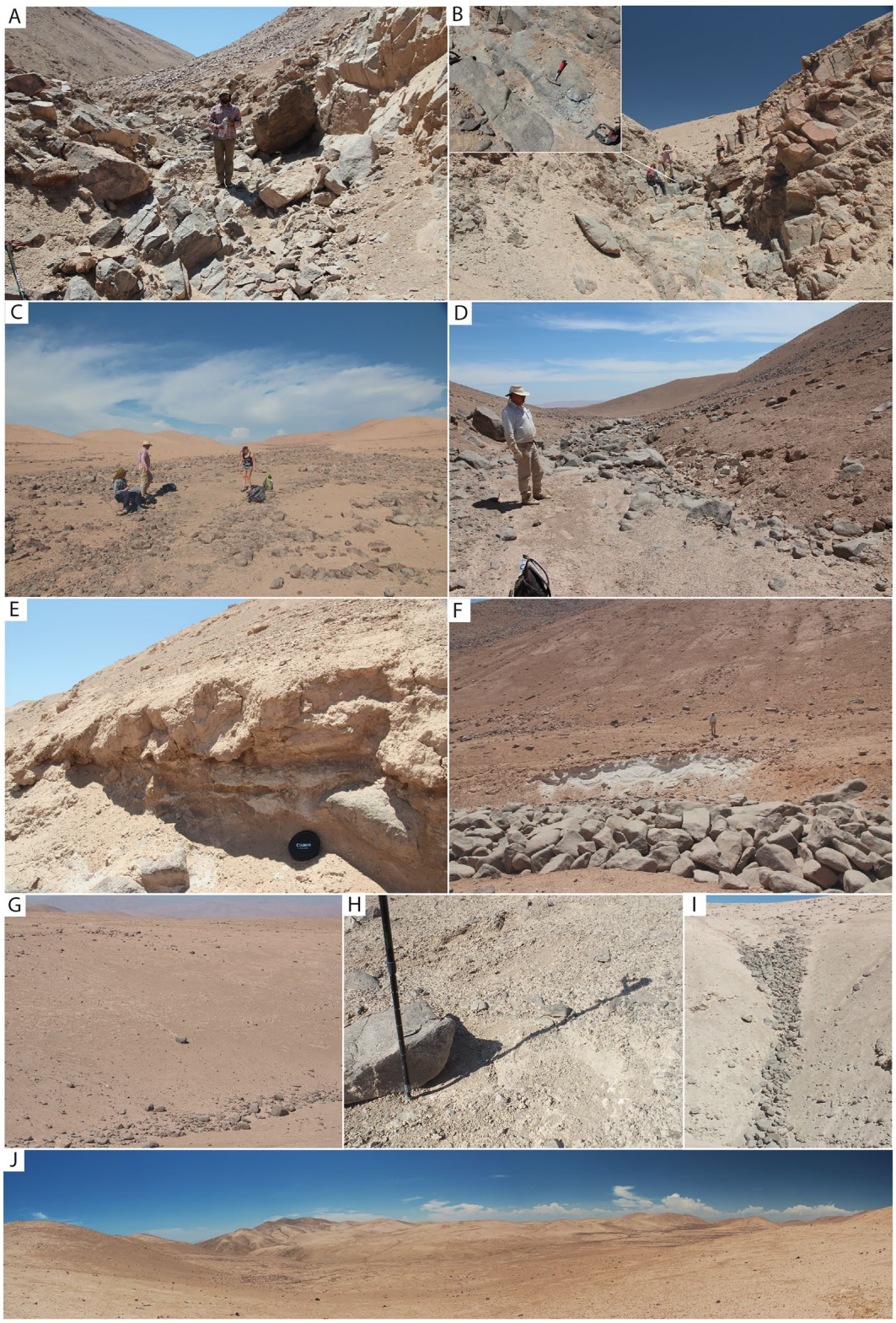

Figure 4.

3. Materials and Methods

3.1. Sampling

For this study, we sampled sediments from 11 channels (SC-S1-2, CC-S1-2, and NC-S1-7) within the HIC along with three bedrock samples at knickpoints (SC-B1, NC-B1, and NC-B2) during field campaigns in 2014, 2015, and 2017. We avoided sediment sampling directly below knickpoints or tributary mouths, as well as close to slope failures. Sediment samples consisted of clastic material with small portions of $CaSO_4$ dust and volcanic glass. Cm-sized thick granodiorite chips were chiseled off from bedrock knickpoints.

Two tephra deposits were sampled to supplement the data set of Vásquez and Sepúlveda (2013) who mapped and dated four tephra deposits within the HIC, with ages ranging from 0.62 to 4.08 Ma (biotite $^{39}Ar/^{40}Ar$). SC-T1 is a thick channel-filling tephra in the SC (Figures 1 and 4f). NC-T1 is located in the NC below NC-S5, deposited in the channel and partly on the adjacent hillslope.

3.2. Analytical Methods

3.2.1. Tephrochronology

Samples taken from tephra deposits were processed using standard mineral separation techniques at the University of Cologne to separate zircon crystals. Single-crystal U-Th/He dating on zircon was applied on one tephra sample (SC-T1) at the University of Göttingen GÖochron Laboratories (Wolff et al., 2021). Zircon from NC-T1 was dated by applying U/Pb dating at FIERCE (Gerdes & Zeh, 2006). A description of the individual dating methods and data is given in the Section S2 in Supporting Information S1) and data set (Ritter et al., 2023).

3.2.2. Cosmogenic Nuclide Erosion Rate Determination

Bedrock samples taken from knickpoints were crushed and sieved to 250–710 µm. Sediment samples were sieved to retain the identical grain-size fraction. All samples were subsequently rinsed, magnetically separated and underwent several density separations to enrich the quartz fraction. The resulting quartz concentrates were investigated under a microscope and, if necessary, manually picked, and subsequently purified by sequential HF-leaching (Kohl & Nishiizumi, 1992). Inductively coupled plasma optical emission spectrometry (ICP-OES) was used to verify that the quartz contained low concentrations of the major elements that can interfere with the sample preparation chemistry or measurement (e.g., Al or Ti) before dissolution.

Etched quartz samples were dissolved following spiking with certified Be (Scharlab, 1,000 mg/l) and Al (Scharlab, 1,000 mg/l) carrier solutions. Accelerator mass spectrometry (AMS) target preparation followed the stacked column approach from S. A. Binnie et al. (2015), coprecipitating Al and Be hydroxides with Ag following Stone et al. (2004). Chemical blanks were prepared alongside the samples. $^{10}Be/^{9}Be$ and $^{26}Al/^{27}Al$ values were measured on CologneAMS (Dewald et al., 2013) in tandem with the prepared chemical blanks. $^{10}Be/^{9}Be$ ratios were normalized to the ICN standard dilution series (Nishiizumi et al., 2007) and $^{26}Al/^{27}Al$ ratios were normalized to the ^{26}Al AMS standards provided by Nishiizumi (2004). For $^{26}Al/^{27}Al$ samples, stable Al contents of the dissolved, spiked samples were determined using ICP-OES and standard addition (4 aliquots) in tandem with quality control measurements of NIST SRM165a. Blank corrected concentrations of ^{10}Be and ^{26}Al were derived following the equations outlined in S. A. Binnie et al. (2019). The uncertainties in the final concentrations are the propagated uncertainties of the AMS ratios of both the sample and the appropriate blank together with the estimated standard deviation of the ^{9}Be or ^{27}Al that the samples contained after spiking.

TCN erosion rates were calculated using the online calculator described in Balco et al. (2008), formerly known as the CRONUS-Earth online calculator (Version 3, https://hess.ess.washington.edu/math/v3/v3_erosion_in.html). We applied the LSDn scaling scheme after Lifton et al. (2014), assuming a bedrock density of 2.85 g/cm³

Figure 4. Compilation of field photographs (Source Benedikt Ritter). (a) northern catchment (NC) bedrock sampling site NC-B2. (b) NC bedrock sampling site NC-B1. (c) NC sampling site NC-S5. This site is relatively flat, comparable to the adjacent Pampa de Perdiz to the west, indicating no signs of recent attempts to adjust to the lower base level. (d). Southern catchment (SC) sampling site SC-S2. (e) Tephra in the NC located within the hillslope deposits. (f) Tephra sampling site SC-T1 in the SC, outcropping further upstream of the sampling point (SC-S1). This tephra is deposited as a thick unit within the main channel throughout this catchment. (g) Observed gravitational sliding of larger boulders, presumably initiated by frequent earthquakes. (h) Sliding mark of the boulder. (i) Boulder accumulations within smaller rills on the hillslopes. Transport of these boulders could be purely gravitationally driven into topographic lows. (j) Panorama view of the flat plateau of the NC, revealing a smooth landscape shaped by diffusive hillslope processes without signs of strong erosion or adaption to the recent base level. On the left of the image is the major channel incising due to adaption to the recent base level drop downstream.

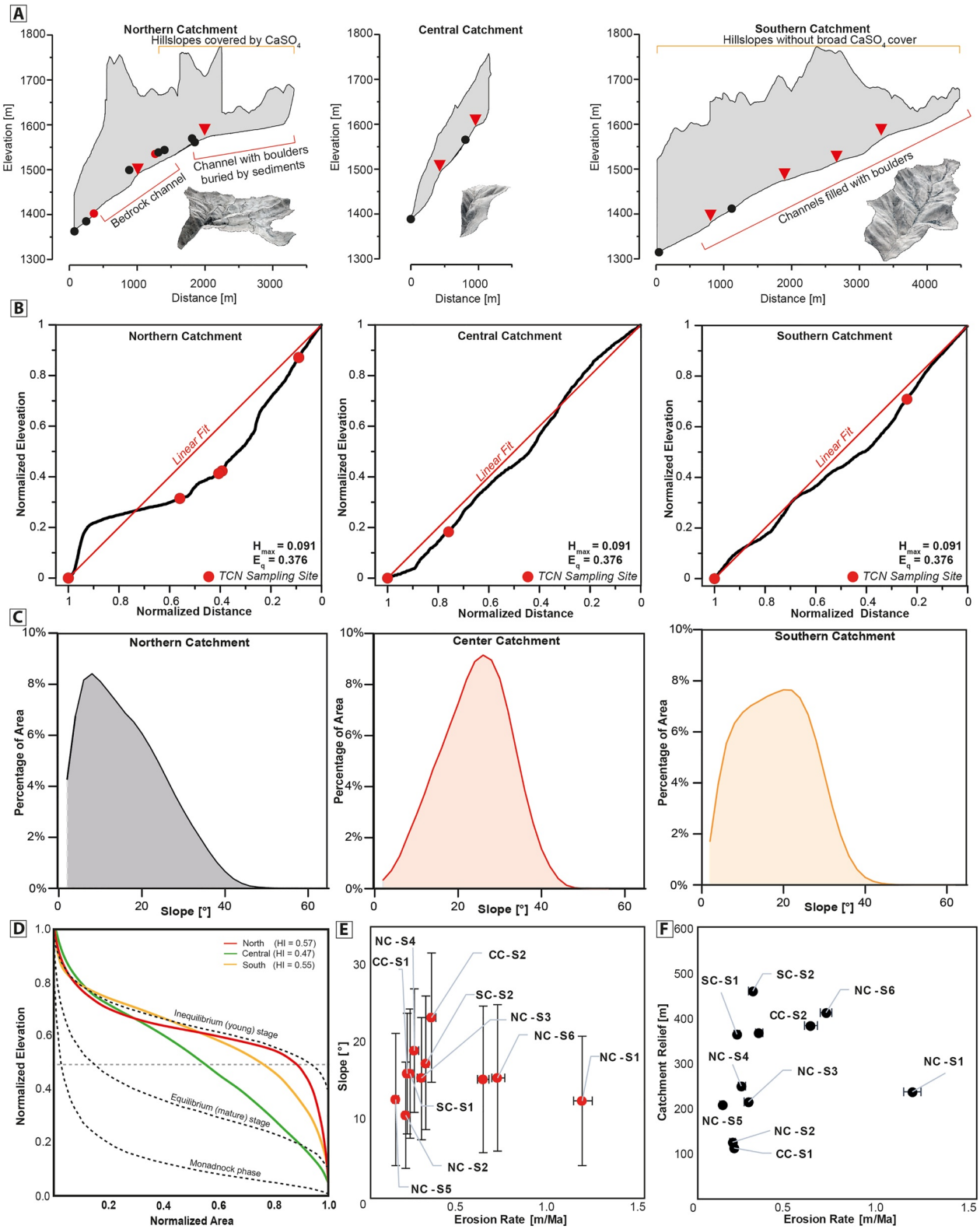
A
Northern Catchment
Hillslopes covered by CaSO4
Channel with boulders buried by sediments
Bedrock channel
Central Catchment
Southern Catchment
Hillslopes without broad CaSO4 cover
Channels filled with boulders
Elevation [m]
Distance [m]
B
Northern Catchment
Central Catchment
Southern Catchment
Linear Fit
Normalized Eleveation
Normalized Elevation
Normalized Distance
Hmax = 0.091
Eq = 0.376
TCN Sampling Site
C
Northern Catchment
Center Catchment
Southern Catchment
Percentage of Area
Slope [°]
D
North (HI = 0.57)
Central (HI = 0.47)
South (HI = 0.55)
Inequilibrium (young) stage
Equilibrium (mature) stage
Monadnock phase
Normalized Elevation
Normalized Area
E
NC-S4
CC-S1
CC-S2
SC-S2
NC-S3
NC-S6
NC-S1
SC-S1
NC-S2
NC-S5
Slope [°]
Erosion Rate [m/Ma]
F
SC-S1
SC-S2
NC-S6
CC-S2
NC-S4
NC-S3
NC-S1
NC-S5
NC-S2
CC-S1
Catchment Relief [m]
Erosion Rate [m/Ma]

Figure 5.

(granodiorite), resulting in an attenuation path length of ~56 cm. This approach only accounts for spallogenic nuclide production, which in very/extremely slowly eroding environments represents the majority of the total ^{10}Be and ^{26}Al production in quartz (e.g., Dunai, 2010). Topographic shielding was calculated from our 1 m DTM (see below) using the ArcMap Toolboxes for catchment-wide (Li, 2013) and discrete samples (Li, 2018). Two-isotope plots (^{26}Al/^{10}Be vs. ^{10}Be concentration) and normalized nuclide concentrations and ^{26}Al/^{10}Be ratios were derived using iceTEA (Jones et al., 2019) open-access script on Matlab (R2021a), that was modified for our calculations (see Section S2 in Supporting Information S1).

3.2.3. DTM- and Satellite Imagery-Based Data Analysis

Larger scale geomorphological analysis of the entire HIC (Figure S1 in Supporting Information S1) is based on SRTM Digital Elevation Model (DEM) data (30 m resolution, Farr et al., 2007), whereas Pléiades 1B satellite imagery (recording date: 17 April 2014; ground resolution: 0.5 m; panchromatic band, http://pleiades.stoa.org/) was used for high-resolution topographic profiles and geomorphological analysis (Figures 3, 5, and 7, Figure S2 in Supporting Information S1). DEM calculation and orthorectification of pansharpened multispectral imagery was conducted using Geomatica (Banff 2020-01-07, PCI). DEM calculation and orthorectification of pansharpened multispectral imagery was conducted using Geomatica (Banff 2020-01-07, PCI). Tie point identification between the two stereo images was conducted automatically and the result was manually edited afterward (X, Y, Z RMS for $n = 64$ tie points: 0.065/0.13, 0.014 m/0.03 px, and 0.011 m). Likewise, additional ground control points ($n = 30$; X, Y, Z RMS = 0.135, 0.134, and 0.497 m) were automatically collected using Fast Fourier Transform Phase matching, and based on an orthorectified image created from the Pléiades images (obtained using the Geomatica software). The GCPs were elevation-corrected using the global TanDEM-X terrain model (12 horizontal and mostly better than 2 m vertical resolution). Due to the absence of vegetation or artificial features in our study area, we consider the derived DEM as a DTM without any further processing.

The final DTM has a resolution of 1 m. Postprocessing using ArcMap (Version 10.6) included smoothing applying a 5 × 5 m moving window. ArcMap was also used to delineate catchment areas, mean elevations, swath profiles, as well as to calculate catchment-averaged geomorphological metrics such as slope, relief, and hilltop curvature. The DTM and satellite imagery were further used to map bedrock outcrops, surface covers, and to trace tectonic fault scarps. Hypsometric curves, that is, normalized elevation-area distributions of each studied catchment, and the corresponding integrals (Hypsometric Integral [HI]) were calculated after Strahler (1957). Furthermore, normalized stream profiles were generated (Figure 5b). Such profiles can yield information on the tectonic setting in which the stream is located in, for example, based on the concavity of the longitudinal profile (Demoulin, 1998). The degree of profile concavity is defined as the maximum distance between an assumed straight original river profile (linear fit to endpoints) and the normalized stream profile (H_{max}) (Demoulin, 1998). The profile concavity, and the position E_q (position of maximal concavity) of H_{max} (degree of profile concavity) in terms of normalized distance to the upstream area, can be used to characterize the concavity of a given stream (Demoulin, 1998).

4. Results

4.1. Tephrochronology

U/Pb dating of zircon grains from NC-T1 provided a mean age of 0.93 ± 0.14 Ma (±2σ, $n = 16$). The mean (U-Th)/He zircon age of SC-T1 (1.17 ± 0.12 Ma, ±2σ, $n = 10$) is comparable with the U/Pb age of NC-T1. Further details about the tephra dating results are given in Section S3 in Supporting Information S1 and data set (Ritter et al., 2023).

4.2. TCN Erosion Rates

Blank corrected concentrations of ^{10}Be and ^{26}Al for sediment samples range from 3.90×10^6 to 1.39×10^7, and from 1.76×10^7 to 4.99×10^7 atoms g^{-1}, respectively (Figure 6, Table 1). Bedrock concentrations of ^{10}Be and ^{26}Al are lower, ranging from 3.65×10^5 to 2.18×10^6, and from 2.36×10^6 to 1.27×10^7 atoms g^{-1}, respectively

Figure 5. (a) Swath profiles (minimum and maximum elevation) along the major axis of all three investigated catchments (based on 2 m Pléiades-1B digital terrain model). Red dots indicate bedrock terrestrial cosmogenic nuclide (TCN) sampling sites and black dots indicate sampling sites for catchment-wide TCN. Red triangles mark knickpoints based on swath-profile elevation data. (b) Normalized longitudinal profiles after Demoulin (1998). (c) Slope-frequency distribution of all three catchments. (d) Hypsometric curves of the three studied catchments and type curves from Strahler (1957), showing the three major geomorphic development stages: young, mature, and Monadnock phases. HI = Hypsometric Integral. Dashed lines indicate the altitudes of the transition from fluvial to diffusive dominant transport/erosional regime. (e) Catchment-wide ^{10}Be erosion rates plotted against slope and (f) catchment relief.

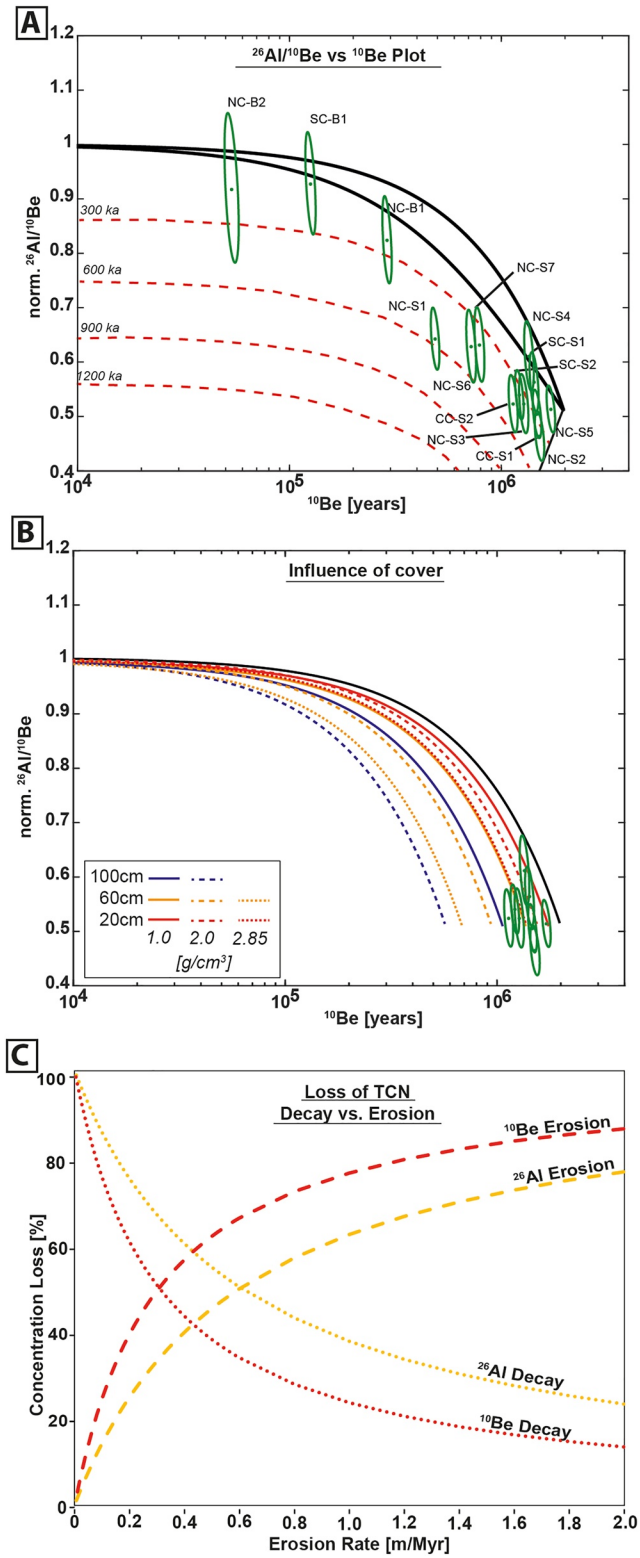

Figure 6.

(Table 1). The ^{10}Be blank corrections amount to <1% for all samples except NC-B2, which has 2.2% of the total measured concentration subtracted. All ^{26}Al blank subtractions equate to <1% of the total concentration measured. ^{26}Al/^{10}Be ratios of the sediment samples indicate a certain degree of intermittent burial/storage of sediments

Table 1
Terrestrial Cosmogenic Nuclide Concentrations, Calculated Maximum Erosion Rates (^{10}Be Max. Erosion, ^{26}Al Max. Erosion), Minimum Exposure Ages (^{10}Be Min. Exp. Age; ^{26}Al Min. Exp. Age), and Normalized ^{26}Al/^{10}Be Ratio (Norm. ^{26}Al/^{10}Be Ratio)

ID	^{10}Be ($\times 10^7$ at/g)	^{26}Al ($\times 10^7$ at/g)	^{10}Be max. erosion (m/Myr)	^{10}Be min. exp. age (Ma)	^{26}Al max. erosion (m/Myr)	^{26}Al min. exp. age (Ma)	Norm. ^{26}Al/^{10}Be ratio
SC-S1	1.12 ± 0.04	4.43 ± 0.25	0.21 ± 0.03	1.66 ± 0.17	0.30 ± 0.09	1.09 ± 0.20	0.56 ± 0.04
SC-S2	0.94 ± 0.03	3.55 ± 0.18	0.30 ± 0.04	1.33 ± 0.13	0.49 ± 0.10	0.82 ± 0.13	0.54 ± 0.03
SC-B1	0.08 ± 0.00	0.54 ± 0.03	4.97 ± 0.37	0.12 ± 0.01	4.97 ± 0.58	0.12 ± 0.01	0.93 ± 0.07
CC-S1	1.18 ± 0.04	4.17 ± 0.22	0.20 ± 0.03	1.75 ± 0.19	0.37 ± 0.09	0.97 ± 0.16	0.50 ± 0.03
CC-S2	0.89 ± 0.03	3.26 ± 0.19	0.33 ± 0.04	1.23 ± 0.11	0.58 ± 0.12	0.74 ± 0.11	0.52 ± 0.04
NC-S1	0.39 ± 0.01	1.76 ± 0.10	1.16 ± 0.10	0.46 ± 0.04	1.62 ± 0.22	0.30 ± 0.04	0.64 ± 0.04
NC-B1	0.22 ± 0.01	1.27 ± 0.07	1.95 ± 0.15	0.28 ± 0.02	2.09 ± 0.27	0.25 ± 0.03	0.82 ± 0.05
NC-S2	1.21 ± 0.04	3.95 ± 0.23	0.19 ± 0.03	1.79 ± 0.20	0.43 ± 0.10	0.89 ± 0.15	0.46 ± 0.03
NC-S3	1.03 ± 0.04	3.79 ± 0.23	0.27 ± 0.04	1.40 ± 0.14	0.48 ± 0.11	0.84 ± 0.14	0.52 ± 0.04
NC-S4	1.08 ± 0.04	4.62 ± 0.28	0.24 ± 0.04	1.53 ± 0.16	0.28 ± 0.09	1.14 ± 0.22	0.61 ± 0.04
NC-S5	1.39 ± 0.05	4.99 ± 0.25	0.13 ± 0.03	2.22 ± 0.27	0.24 ± 0.08	1.23 ± 0.24	0.51 ± 0.03
NC-S6	0.57 ± 0.02	2.52 ± 0.16	0.69 ± 0.07	0.74 ± 0.06	0.95 ± 0.16	0.50 ± 0.07	0.63 ± 0.04
NC-S7	0.63 ± 0.02	2.77 ± 0.18	0.61 ± 0.06	0.81 ± 0.07	0.81 ± 0.15	0.55 ± 0.08	0.63 ± 0.05
NC-B2	0.037 ± 0.002	0.24 ± 0.02	12.20 ± 0.98	0.052 ± 0.004	12.80 ± 1.62	0.05 ± 0.01	0.92 ± 0.09

Note. Further details for the calculation are listed in Supporting Information S1. All uncertainties are ±1 standard deviation (external uncertainty).

within the catchment according to their position in the ^{26}Al/^{10}Be-^{10}Be plot (Figure 6a). The data set is stored in Supporting Information S1 and database (Ritter et al., 2023). Once a sample is buried beneath significant overburden (on the order of several meters), the ratio of ^{26}Al/^{10}Be is controlled by the radioactive decay of both isotopes. As ^{26}Al is decaying faster than ^{10}Be, the sample will plot below the steady-state erosion island (Dunai, 2010).

Assuming that the sampled sediments have been continuously exposed at the Earth's surface without any loss of nuclides due to decay by burial, basin-averaged apparent (i.e., maximum; see Section 5) erosion rates inferred from ^{10}Be and ^{26}Al concentrations are on the order of <2 m/Myr (minimum exposure age >250 ka), with the majority being <1 m/Myr (equivalent minimum exposure age >500 ka, Figure 7, Table 1). In most sediment samples, however, basin-averaged erosion rates inferred from ^{26}Al concentrations regularly exceed those inferred from ^{10}Be by up to 45%. The timescales over which the erosion rates integrate T_{ave} (i.e., the time to remove the uppermost ∼56 cm of bedrock, assuming spallation dominated production) differ by one order of magnitude between basin-averaged erosion rates from sediment samples and bedrock samples (Supplementary). Basin-averaged erosion rates obtained from slowly eroding catchments integrate over ∼1 to almost ∼4 Myr, those in faster eroding parts (especially bedrock) over the last ∼50–∼500 kyr (Section S3 in Supporting Information S1).

Maximum basin-averaged erosion rates (^{26}Al, ^{10}Be) in the SC are in the order of <0.5 m/Myr; a slight downstream increase in the erosion rate can be observed. ^{10}Be basin-averaged maximum erosion rates are <0.3 m/Myr. In contrast, the bedrock erosion rate is up to 5 m/Myr. In the central catchment, we also measure low basin-averaged maximum ^{26}Al erosion rates (<0.6 m/Myr), with ^{10}Be basin-averaged maximum erosion rates on the order of <0.3 m/Myr. The NC appears to host two erosion regimes. Low basin-averaged maximum erosion of

Figure 6. Two-isotope plot showing ^{26}Al/^{10}Be ratios versus. log ^{10}Be [years] concentrations of sediments and bedrock samples. Ellipses display 1σ uncertainty. (a) Continuously exposed samples should coincide, within uncertainties, with the steady-state erosion island, defined as the area between the upper and lower black curves representing continuous exposure and steady-state erosion, respectively. Red dashed lines indicate burial isochrons. (b) Calculated continuous exposure isolines representing the effects on concentrations of different thicknesses (0–100 cm) and densities of the covering material (1.0 and 2.0 g/cm^3). (c) Relative contributions by decay and erosion to the ^{26}Al or ^{10}Be concentration when erosion rates are low. In the application of the basin-wide approach to determine erosion rates with terrestrial cosmogenic nuclide, the dominance of decay versus erosion in controlling the concentration at very low erosion rates biases the rates toward the most rapidly eroding parts of the catchment (Granger et al., 2001). The intersection point at which the loss due to decay dominates the concentration is higher for the ^{26}Al system (∼0.6 m/Myr) than for the ^{10}Be system (∼0.3 m/Myr).

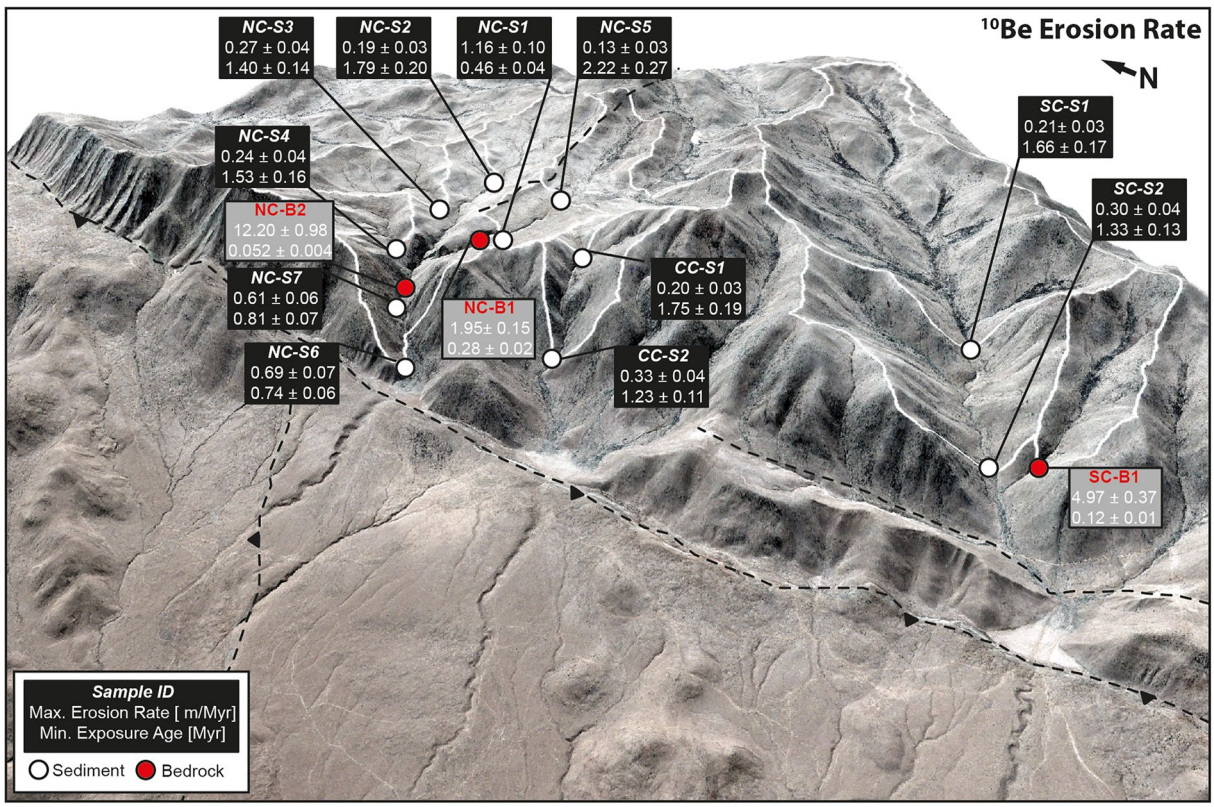

Figure 7. 3D-scene based on Pléiades-1B digital terrain model (2 m resolution) and pansharpened multispectral image (Pléiades-1B), vertical exaggeration 2x (created using ArcGIS Pro 2.8.1—pro.arcgis.com—and Adobe Illustrator 2022—adobe.com). Compilation of derived terrestrial cosmogenic nuclide catchment-wide maximum ^{10}Be erosion rates and bedrock erosion rates (in m/Myr), and ^{10}Be minimum exposure ages (in Ma). Bedrock ^{10}Be erosion rates are up to five times higher than most of the catchment-wide erosion rates. Calculated reach erosion rates for the respective subcatchments are illustrated.

<0.3 m/Myr (Figure 7) is measured in the upper reaches of the catchment, while the total basin-averaged erosion rate is on the order of <1.2 m/Myr. Bedrock erosion rates in the NC are between 2 and 12 m/Myr (NC-B1-B2).

4.3. Geomorphic Metrics—Hypsometry

The generated normalized stream profiles yield values for H_{max} of 0.097 (SC), 0.069 (Central Catchment), and 0.185 (NC), which correspond to values for E_q of 0.376, 0.892, and 0.392, respectively (Figure 5b). As such, all profiles strongly differ from those of well-graded streams commonly associated with fluvial systems in equilibrium (Leopold & Bull, 1979), where H_{max} and E_q may approach values closer to 0.3 (Demoulin, 1998). As reflected by the values for H_{max}, the southern and central catchments have almost linear normalized stream profiles, indicating strong tectonic activity governing surface processes in these catchments (Demoulin, 1998). The longitudinal profile of the NC shows a larger concavity in the upstream area, turning into a strongly convex zone in the lower portion. The transition from a concave to a convex profile spatially coincides with the knickpoint located at NC-B1 and hence reflects the transition between two erosional regimes governed by tectonic uplift. Catchment slope-frequency distributions display unimodal distributions (Figure 5c). The NC, however, indicates a right-skewed distribution reflecting the lower relief upper parts of the catchments with a mean slope of ∼15°. The central catchment indicates a symmetric normal distribution with a mean slope of ∼24°, presumably due to the small catchment size. The SC reveals a mean slope of ∼17° and a much broader, almost plateau-shaped distribution.

The low basin-averaged erosion rates that we obtain do not show any relation with geomorphic metrics, such as local relief or mean slope (Figures 5e and 5f). Lowest basin-averaged erosion rates coincide with comparably steep slopes and high reliefs. TCN erosion rates do not reflect variations of relief between ∼100 and 450 m, and 5°–22.5° (sub) catchment-averaged hillslope angles. Higher erosion rates of NC-S7 and NC-S6, however, correspond to a higher channel gradient. Samples from the central catchment (CC-S1-2) reveal extremely low erosion rates (<0.6 m/Myr), despite the high topographic gradients within the catchment. Comparing catchment erosion

rates derived here with their mean hillslopes and relief indicates that these parameters are unrelated, indicating a disconnect between topographic form and surface activity.

All catchments indicate rather high HI values, reflecting that large parts of their surface remain at high altitudes (Figure 5d). Consequently, hypsometric curves of the southern and northern catchments can be regarded as a juvenile stage of geomorphic development, while the central catchment hypsometric curve displays a more intermediate geomorphic development (Strahler, 1957) (Figure 5d). Geomorphometric data are stored in Supporting Information S1 and data set (Ritter et al., 2023).

5. Interpretation and Discussion

Basin-averaged erosion rate estimates from TCNs use an idealized model of erosional processes, which requires a set of assumptions to be fulfilled (Granger et al., 2001; Von Blanckenburg, 2005). However, in extreme environments, such as the Atacama Desert, some of these assumptions might be violated, which, however, can be identified using paired cosmogenic nuclides (Campbell et al., 2022). The following section will consider the sensitivity of TCN-derived erosion rates to processes particular to hyperarid environments.

Our TCN concentrations indicate that extremely low basin-averaged erosion rates presumably prevailed since the Plio/Pleistocene in parts of the studied catchments, based on T_{ave}, the time to remove one attenuation path length (~56 cm, average ^{10}Be T_{ave} ~2.3, average ^{26}Al T_{ave} ~1.4 Ma (Dunai, 2010; Lal, 1991), see Section S3 in Supporting Information S1) and by the position on the two-isotope plot (high ^{10}Be concentrations indicate long-term exposure, consequently, samples lie to the right in the plot of Figure 6a). Major assumptions that should be fulfilled when deriving basin-averaged erosion rates from TCN concentrations include steady-state erosion for the removal of up to 4–5 attenuation lengths of unexposed material (Lal, 1991) and subsequent negligible sediment transport times to the channel after detachment from the hillslopes, that is, (e.g., Bierman & Steig, 1996). These assumptions might not be fulfilled in our study area, as we observed indications for long-term sediment storage, primarily in the lower reaches of the NC at the transition zone from the plateau-like upstream area toward the deeply incised reaches. Storage of detached bedrock material on the slopes or in channels for periods in excess of a few hundred thousand years (in the case of ^{10}Be and ^{26}Al) violates assumptions inherent in the conceptual TCN-based erosion rate model (Bierman & Steig, 1996). The observed downstream increase in the deviation of the ^{26}Al/^{10}Be ratio from the steady-state island, such as evident for NC-S1, can be attributed to increased tapping of sediment from storage (<3 m) with long or repeated burial histories. In theory, such a scenario could provide a simple explanation for the deviation of ^{26}Al/^{10}Be ratios from the steady-state island (Figure 6a). However, field evidence indicates that some samples have complex TCN histories, which cannot be explained by the recycling of deeply buried sediments (no indication of erosion from stored material upstream of SC-S1-2, CC-S1-2, and NC-S2-5). Hence, in these cases, the calculated apparent burial durations derived from Figure 6a should be simply regarded as a measure for the deviation from the steady-state ^{26}Al/^{10}Be ratio. Potential processes which cause the deviation of ^{26}Al and ^{10}Be concentrations will be discussed in the following.

5.1. High TCN Concentrations—Depth Dependency of Production Versus Decay

The concentration of a given cosmogenic radionuclide at a surface undergoing long-term steady state erosion is governed by the rates of nuclide production, nuclide decay, and the erosion rate of the surface (Lal, 1991). With increasing depth below the surface, however, the subsurface nuclide production decreases, and thus the decay increasingly exerts dominant control on the nuclide concentration. The depth-dependency of the nuclide production becomes less pronounced with increasing nuclide concentration as radioactive decay becomes more important relative to the production rate (Struck et al., 2018; Wittmann & von Blanckenburg, 2009). Under such conditions, ^{26}Al/^{10}Be ratios will start to decrease through the profile due to the faster decay of ^{26}Al. Under conditions of slow erosion, as found in our study, the ^{26}Al concentration of a given parcel of subsurface bedrock moving toward the surface due to erosion could have attained secular equilibrium, independent from the surface erosion rate, whereas the ^{10}Be concentration continues to increase. Assuming a weathering-limited environment with outcropping bedrock/regolith at the surface and that the production of cosmogenic nuclides in the subsurface is modulated by the density of the bedrock (2.85 g/cm³), rapid mobilization and especially mixing of material from the near-surface (depths of less than 10 cm) could explain the deviation of the measured ^{26}Al/^{10}Be ratio from the steady-state erosion line (Figure 6b).

5.2. Impact of Atmospheric Deposition on TCN Concentration in Sediment Samples

This simplified shallow mixing model might be insufficient in extreme hyperarid transport-limited environments, as the formation of soils (Struck et al., 2018) and additional impacts of atmospheric deposition increase the rock/sediment column and thus might interfere/violate the general erosion model. Bedrock outcrops in the upper reaches of the studied catchments are rare (Figure 3b), indicating that detached grains from bedrock are not simply affected by the attenuation of the density of the regolith and bedrock alone (see above) but additionally by soil accumulation due to atmospheric deposition (Michalski et al., 2004; Rech et al., 2019; Wang et al., 2015). The significant soil cover (observed: up to 80 cm) increases the (partially) shielded residence time of grains on the hillslopes on their transit to the channels. This holds independent of the process of moving the soils and entrained bedrock material to the channels (mass flow, slump, creep; i.e., well mixed or retaining stratification; e.g., Figures 3b and 3c).

Dust deposition rates from the Atacama Desert based on meteoric ^{10}Be data (Wang et al., 2015) indicate atmospheric deposition rates of the order 30–40 cm/Myr. The densities of $CaSO_4$-rich soils within the Atacama Desert range between 1 and 2 g/cm^3 (e.g., Ewing et al., 2006; Pfeiffer et al., 2021; Wang et al., 2015). We modeled the effect of sediment cover mimicking a $CaSO_4$-rich soil to illustrate its potential effect on the TCN inventory (Figure 6a). For this modeling approach, we focused on samples (SC-S1 to 2, CC-S1 and 2, NC-S2 to 5, Figures 2 and 3) in the upper reaches of the catchment. The attenuation correction factor (f_{cover}) of subsurface production of cosmogenic nuclides was modeled for densities between 0.5 and 3.0 g/cm³ (beyond the densities for Atacama soils, including bedrock density) and various depths (0–120 cm), which cover the potential conditions observed in our catchment areas (Figure 6b and Figure S3 in Supporting Information S1). For instance, cover thicknesses of 20–30 with a mean density of 2.0, of ∼20–40 with a density of 1.5, or 50 cm with a density of 1.0 g/cm³ can explain the position of our samples in ^{26}Al/^{10}Be versus ^{10}Be space (Figure 6b), assuming they spend most of their time on the hillslopes in (partially) shielded position before entering the channel. Material transport to the channels by creep and slumping (e.g., Figures 3b and 3c) are compatible with this assumption. Mass flow would violate it; however, the catchments are devoid of visible traces of mass flow events on the hillslopes. The values we assume for surface cover are typical for the core region of the Atacama Desert (Ericksen, 1981; Ewing et al., 2006; Wang et al., 2015). Consequently,^{10}Be derived erosion rates from channel sediments in the region might experience similar effects, which go undetected, when using one isotope only.

5.3. Cosmogenic Nuclide Derived Erosion Rates Close to Secular Equilibrium of Radiogenic ^{26}Al—^{10}Be

We calculate rather low basin-averaged erosion rates from our ^{26}Al and ^{10}Be concentrations, meaning that radiogenic decay cannot be ignored and one of the assumptions used for calculating basin-averaged nuclide-derived erosion rates might be violated (Bierman & Steig, 1996). The rates in slowly eroding parts of a catchment are underestimated in such environments due to a partial loss of the erosion signal by decay, violating the assumption of an equitably produced signal from the entire catchment. Therefore, the inferred basin-average erosion rate will be biased to higher values, inadequately representing slower eroding parts of a basin (Granger et al., 2001) (Figure 6c). This bias is more pronounced for the shorter-lived ^{26}Al as compared to ^{10}Be. Erosion rates in excess of around 0.3 (^{10}Be, Granger et al., 2001) and around 0.6 m/Myr (^{26}Al, von Blanckenburg, 2005) minimize this bias. Many of the calculated basin-averaged erosion rates in our study area are close to or beneath these lower limits (Figure 6a, Table 1). The low ^{26}Al/^{10}Be ratios we find for samples from the upper catchments, which are all within uncertainty at the point of saturation (Figure 6b), require erosion rates below 0.1 m/Myr. Since we are biased to higher rates (Granger et al., 2001), this is an upper limit. In the following section, to simplify the discussion and maintain comparability with previous studies, we use the calculated ^{10}Be erosion rates as conservative estimates of the erosion rate.

5.4. Independent Erosion Rate Constrains

Dated tephra deposits yield U/Pb (NC-T1) and U-Th/He (SC-T1) ages of approximately ∼1 Ma (supplementary). Other tephra deposits of similar age or older have been mapped by Vásquez and Sepúlveda (2013) in the vicinity of our study area. The preservation of easily erodible tephra deposits outcropping at the rims or hillslopes of fluvial channels (Figures 4e and 4f) indicates that these deposits have not been subject to notable erosion since at least ∼1 Ma. The erosion of the tephra-deposits we observed were all linked to channel erosion (Figure 4f).

Located at the outlet of the SC, Diederich et al. (2020) investigated a short sediment core and seismic data from an endorheic clay pan. A rough extrapolation with the published age-depth model (~4 m depth, basal age of ~68 ka), the clay pan size (~0.12 km^2), the potential maximum depth of the sedimentary infill from seismic data (30–40 m) and the catchment size of the entire SC (~12 km^2), and assuming that the entire catchment equally contributed to the filling of the clay pan, an erosion rate of ~0.4 m/Myr can be approximated (bedrock density 2.85, sediment infill 2.0 g cm^{-3}). For the calculation, an oversimplified triangular box for the sedimentary basin was assumed. Therefore, the sedimentary infill is likely to be overestimated, that is, the approximated erosion rate reflects a maximum value and could be considerably lower than calculated. The crudeness of the calculations notwithstanding, this erosion rate is in good agreement with the rates derived from cosmogenic nuclides (Table 1, Figure 7).

Basin-averaged erosion rates derived in this study are at the lower end of published rates from the Atacama Desert, most likely due to the location of our catchments within the hyperarid core of the desert. While other studies found higher rates at the fringes of the hyperarid core (Mohren et al., 2020; Starke et al., 2017), low rates of about ~1 m/Myr are found within the Coastal Cordillera (Mohren et al., 2020; C. Placzek et al., 2014) and the southern extents of the desert (Nishiizumi et al., 2005). Mohren et al. (2020) have shown that such low rates can be maintained despite high elevational gradients induced by geologically recent (Mid Pleistocene) base-level lowering. High TCN concentration clearly demonstrate a predominant hyperarid climate during the past few millions of years in our study area.

5.5. Bedrock Erosion Rates Contrast Low Basin-Averaged Erosion Rates

TCN-derived bedrock channel erosion rates are one to two orders of magnitude higher (2–12 m/Myr) than basin-averaged erosion rates (<1 m/Myr, Table 1, Figure 7). More rapid bedrock channel erosion rates in relation to much lower upstream basin-averaged erosion rates of regolith mantled hillslopes are illustrative of the intra-catchment transition between different erosional regimes (Crosby & Whipple, 2006). The contrasting erosion and deposition milieus of the upstream knickpoint area versus the downstream area, that is, high-altitude low relief and transport-limited environment versus the bedrock channel, high relief, weathering limited environment, are indicative of this transition. From a geomorphological perspective, the notion of bedrock knickpoint migration, or lack thereof, governing lower erosion rates further upstream is typical of a predominantly bottom-up controlled system (Bishop, 2007). Higher bedrock erosion rates in the channels suggest the importance of tectonic forcing for landscape evolution in our study area via uplift-induced base-level change. The upstream areas, which appear to be in a state of long-term stasis, have yet to adapt to the new boundary conditions communicated to the lower portions by the knickpoints.

The comparison of basin averaged erosion rates may be affected by a grain-size bias if higher altitudinal parts of steep catchments produce larger grain-size, which are subsequently unrepresented in samples of sand grain-size (Lukens et al., 2016). However, in our study area, the topography of the catchments is the opposite of the more typical case discussed in Lukens et al. (2016). In our case, the lower catchment areas are steeper compared to the flatter upper areas, such that the grain-size of transported material does not increase with elevation. Consequently, the potential bias described in Lukens et al. (2016) does not pertain to the present study.

The patterns of higher channel sediment TCN concentrations versus lower bedrock concentrations contrast some of the results presented in the study of C. Placzek et al. (2014), who comprehensively analyzed both sample types in the arid to hyperarid Atacama Desert (eastern and interior Coastal Cordillera, ~22°–25°S). In contrast to C. Placzek et al. (2014), basin averaged erosion rates from channel sediments in our study area reveal much higher TCN concentrations than bedrock TCN concentrations. Although erosion rates obtained in our study are in the same order of magnitude for basin averaged erosion rates (0.6–2.5 m/Ma, C. Placzek et al. (2014)), bedrock erosion rates from bedrock knickpoints in our study area are at the upper end of reported erosion rates by C. Placzek et al. (2014). Isolated surface boulder erosion rates (bedrock) investigated by C. Placzek et al. (2014) represent mostly weathering-dominated erosion and not, to a large extent, erosion due to fluvial activity (running water with sediment load).

Bedrock erosion rates determined from spatially dispersed outcrops protruding from the crests of hillslopes (1.5–5.0 m/Myr ^{10}Be recalculated using applied calculation scheme in this study, Nishiizumi et al., 2005) can provide insights into the magnitude of diffusive surface processes, that is, the downwearing of topography under

arid to hyperarid climates. Hillslope bedrock erosion rates from Kober et al. (2007) obtained from sampling sites in the Western Cordillera indicate much higher bedrock erosion rates (up to 46 m/Myr). In contrast, TCN erosion rates (24°–27°S) reported by Owen et al. (2011) indicate mainly hillslope erosion rates derived from the bedrock/saprolite interaction zone from soil pits (~1 m/Myr), which represent a different erosion rate compared to basin averaged erosion rates from channel sediments and bedrock erosion rates. Nevertheless, Owen et al. (2011) reported one channel bedrock erosion rate of 1.3 m/Myr (^{10}Be erosion rate with indications of complex burial), which is one of the lowest bedrock channel erosion rates published so far in the Atacama Desert. Our bedrock samples are taken from channel beds in an active tectonic setting, which might explain higher bedrock erosion rates, representing the culmination of advective processes. Similar observations were reported by Mohren et al. (2020), who found bedrock erosion rates further to the south, adjacent to the Río Loa, to be on the order of ~40 m/Myr.

5.6. Landscape Evolution and Dominant Factors Governing Surface Processes

In general, surface activity is extremely low within the HIC catchments (Table 1), which underscores the predominant hyperarid climate since at least the Miocene. Our apparent erosion rates calculated from cosmogenic nuclide concentrations of ^{10}Be and ^{26}Al integrate over the Late Pliocene and Pleistocene (T_{ave} in Section S3 in Supporting Information S1). Beyond that timespan, TCN exposure ages from adjacent and previously connected alluvial fans and fluvial meandering channels directly to the west of the HIC (Ritter et al., 2022) indicate predominantly arid to hyperarid conditions since at least the Early Miocene. Based on surface exposure dating and incorporated tephra deposits within the Alto Hospicio formation (Vásquez & Sepúlveda, 2013), Ritter et al. (2022) concluded that most of the erosional products situated at the foot of the HIC today were delivered as a result of fluvial incision of the HIC prior to or during the Early Miocene. The overall fluvial topography of the HIC was likely formed already before/during the Oligocene to Early Miocene. Younger (Miocene to recent) landscape modification, such as debris flows onto alluvial fan surfaces and more recent fluvial incision into older alluvial fan deposits, are regarded as insignificant contributors to the bulk of fluvial erosion within the HIC.

As the climate has been predominantly hyperarid since at least the Early Miocene, tectonic activity is the major cause of landscape modification by driving base-level changes and consequently increasing relief and slope angles. The latter was indicated by several studies to be the most important factor for initiating surface runoff and erosion during recent rare precipitation events in the hyperarid Atacama Desert (Jordan et al., 2015; May et al., 2020).

Precipitation records covering the observational timescale from the Atacama Desert are scarce (Schween et al., 2020). Exceptional precipitation events in March 2015 (e.g., Bozkurt et al., 2016), January 2020 (Vicencio Veloso, 2022), and March 2022 (Cabré et al., 2022) have received considerable attention. These events mostly occurred several hundred kilometers further south. There are no observational records of extreme rain events in the study area, either due to an observational gap or the long-term absence of such events. One of the most recent rain events in the region, which caused severe damage in the proximal coastal town of Iquique (Vicencio Veloso, 2022), did not affect the study area in the Coastal Cordillera (<1 mm precipitation weather station 23—Cerro Constancia, Hoffmeister, 2018). Rare gravel layers in the 68 ka sediment record in the terminal pan of the southernmost catchment (Diederich et al., 2020) indicate that extreme events (those that can wash gravel onto a flat surface over a distance of ca. 300 m) occur less than once in 10 ka. The same study (Diederich et al., 2020) points to low but steady sedimentation and erosion rates over the last 68 ka. In any case, due to the long half-lives of ^{10}Be and ^{26}Al and the long averaging timescales of the TCN methodology, TCN-derived erosion rates are insensitive to short-term changes in erosion rates (Kirchner et al., 2001).

Areas that are not directly affected by base-level drops near the catchment mouths, such as the upper "plateau" of the NC, have hillslopes mantled by a soil layer enriched in atmospherically deposited $CaSO_4$ that can protect from erosion. Studies conducted in the Atacama Desert (Jordan et al., 2015; May et al., 2020; Pfeiffer et al., 2021) identified the potential of $CaSO_4$-rich soils on rare and/or artificial precipitation events to prevent overland flow by increasing infiltration capacity. Hortonian overland flows may be suppressed by high infiltration capacities, subsequently causing a self-reinforcing mechanism by stabilizing and protecting these covers from any erosion. For the March 2015 event, with locally up to 85 mm/24 hr precipitation, Jordan et al. (2015) found indications that flat-angle hillslopes and surfaces (<7°, based on 90 m SRTM) experienced no measurable surface modifications, thus implying that surficial covers of $CaSO_4$-rich soils may hinder surface activity by absorbing rain.

In the SC, accumulations of interlocking large boulders (several dm to m size; Figure 4f) in the channels armor their beds from erosion, thereby slowing valley incision (see additional information in Section S4 in Supporting Information S1). These boulder accumulations are found as high as the channel heads of tributaries (Figures 3 and 4i). Gravitational hillslope transport, assisted by seismic shaking (Figure 5h, Matmon et al., 2015; May et al., 2019; Quade et al., 2012), is the likely process transporting the boulders in to the channels (see additional information in Section S4 in Supporting Information S1). Seismic shaking would also assist in interlocking the boulders (Figure 4f).

Higher erosion rates in bedrock channels can be best explained by the removal of protective elements, such as sediments and boulder accumulations. Channel slopes are steeper, preventing the accumulation of enough $CaSO_4$-rich soil to reduce the erosional impact of precipitation events. Furthermore, bare bedrock is prone to physical weathering processes driven by high diurnal temperature variability (Min./mean/max. air temperature [2 m]: 2.19°C/16.64°C/28.61°C, Hoffmeister, 2018). Recent soil disc infiltrometer measurements on hillslopes from the southern Atacama Desert revealed that only precipitation exceeding 78 mm/hr was able to saturate soils and infiltration capacity and to initiate overland flow (Pfeiffer et al., 2021). We assume a similar situation for the upper catchments of the current study. In rare events with overland flow, and consequently channel flow, the boulder accumulations we observe in some channels (Figures 3e, 3f, and 4f) will slow the velocity of runoff and thus reduce its erosive capacity. Averaged over long timescales, channel incision is reduced, as is the pace of which adjacent hillslopes adjust (see also Shobe et al. (2021)).

6. Conclusion

Our study addresses the lack of erosion rate studies in the hyperarid Coastal Cordillera of the Atacama Desert and the importance of applying a two-isotope TCN approach in hyperarid environments. The TCN-derived erosion rates indicate that predominantly slow rates of surface activity prevailed in this part of the Atacama Desert during the Pleistocene and likely beyond. As a result, basin-averaged erosion rates are extremely low, even in catchments with steep slopes and high relief. The preservation of early Miocene surfaces in close proximity (Ritter et al., 2022) indicates that low erosion rates have probably prevailed during the entire Miocene. Long-term aridity leads to a partial decoupling of erosion and geomorphological parameters, which has important implications for landscape evolution models in arid to hyperarid environments. Studies in less severely water-limited landscapes have established a positive correlation between mean slope or catchment relief and erosion rates (e.g., S. A. Binnie et al., 2007; Dibiase et al., 2010; Portenga & Bierman, 2011), however, this correlation may not hold for hyperarid landscapes, where topographic slope may be largely decoupled from erosion rates, and significant parts of the landscape are in a form of hibernation. In our specific case, erosive episodes are linked to rare precipitation events exceeding the large saturation and infiltration capacity of calcium sulfate-rich soils. The rarity of these is confirmed by local sediment records (Diederich et al., 2020). Upland channels are, in places, choked with large boulders that reduce the erosive power of runoff during extreme rain events. The boulders are transported from the hillslopes to the channels by gravitational sliding, aided by seismic shaking. The combination of long-term aridity, sulfate-soils, and seismically induced channel obstructions are key factors in preserving a tectonically uplifted landscape.

Conflict of Interest

The authors declare that the research was conducted in the absence of any commercial or financial relationships that could be construed as a potential conflict of interest.

Data Availability Statement

All data generated during this study are included in this published article (and its Supporting Information S1 file), as well as digital data set on the CRC1211 Database (www.crc1211db.uni-koeln.de). Data set Ritter et al. (2023). The data set (excel file .xls) contains tephrochronological data (U-Th-He data of HU14-01, U/Pb data of HU15-07), geomorphic parameters for the studied catchments, as well as, all relevant information for TCN erosion rate determination (AMS Data, TCN erosion rate and apparent exposure age data).

Acknowledgments
Thanks go to Elena Voronina, Damián López, and Tomasz Góral for help processing samples for ^{10}Be and ^{26}Al analysis at the University of Cologne. Finally, we would like to thank Eduardo Campos and colleagues at the Universidad Catolica del Norte at Antofagasta for their patient and essential support. Funded by the Deutsche Forschungsgemeinschaft (DFG, German Research Foundation)—Projektnummer 268236062—SFB 1211. This is FIERCE contribution no. 119. Open Access funding enabled and organized by Projekt DEAL.

References

Aguilar, G., Cabré, A., Fredes, V., & Villela, B. (2020). Erosion after an extreme storm event in an arid fluvial system of the southern Atacama Desert: An assessment of the magnitude, return time, and conditioning factors of erosion and debris flow generation. *Natural Hazards and Earth System Sciences*, *20*(5), 1247–1265. https://doi.org/10.5194/nhess-20-1247-2020

Allmendinger, R. W., & González, G. (2010). Invited review paper: Neogene to Quaternary tectonics of the coastal Cordillera, northern Chile. *Tectonophysics*, *495*(1–2), 93–110. https://doi.org/10.1016/j.tecto.2009.04.019

Balco, G., Stone, J. O., Lifton, N. A., & Dunai, T. J. (2008). A complete and easily accessible means of calculating surface exposure ages or erosion rates from (10)Be and (26)Al measurements. *Quaternary Geochronology*, *3*, 174–195. https://doi.org/10.1016/j.quageo.2007.12.001

Bierman, P., & Steig, E. J. (1996). Estimating rates of denudation using cosmogenic isotope abundances in sediment. *Earth Surfaces and Landforms*, *21*(2), 125–139. https://doi.org/10.1002/(sici)1096-9837(199602)21:2<125::aid-esp511>3.0.co;2-8

Binnie, S., Reicherter, K., Victor, P., González, G., Binnie, A., Niemann, K., et al. (2020). The origins and implications of paleochannels in hyperarid, tectonically active regions: The northern Atacama Desert, Chile. *Global and Planetary Change*, *185*, 103083. https://doi.org/10.1016/j.gloplacha.2019.103083

Binnie, S. A., Dewald, A., Heinze, S., Voronina, E., Hein, A., Wittmann, H., et al. (2019). Preliminary results of CoQtz-N: A quartz reference material for terrestrial in-situ cosmogenic ^{10}Be and ^{26}Al measurements. *Nuclear Instruments and Methods in Physics Research Section B: Beam Interactions with Materials and Atoms*, *456*, 203–212. https://doi.org/10.1016/j.nimb.2019.04.073

Binnie, S. A., Dunai, T. J., Voronina, E., Goral, T., Heinze, S., & Dewald, A. (2015). Separation of Be and Al for AMS using single-step column chromatography. *Nuclear Instruments and Methods in Physics Research Section B: Beam Interactions with Materials and Atoms*, *361*, 397–401. https://doi.org/10.1016/j.nimb.2015.03.069

Binnie, S. A., Phillips, W. M., Summerfield, M. A., & Fiefield, L. K. (2007). Tectonic uplift, threshold hillslopes, and denudation rates in a developing mountain range. *Geology*, *35*(8), 743–746. https://doi.org/10.1130/g23641a.1

Bishop, P. (2007). Long-term landscape evolution: Linking tectonics and surface processes. *Earth Surface Processes and Landforms: the Journal of the British Geomorphological Research Group*, *32*(3), 329–365. https://doi.org/10.1002/esp.1493

Bozkurt, D., Rondanelli, R., Garreaud, R., & Arriagada, A. (2016). Impact of warmer eastern tropical Pacific SST on the March 2015 Atacama floods. *Monthly Weather Review*, *144*(11), 4441–4460. https://doi.org/10.1175/mwr-d-16-0041.1

Cabré, A., Remy, D., Marc, O., Burrows, K., & Carretier, S. (2022). Flash floods triggered by the 15–17th March 2022 rainstorm event in the Atacama Desert mapped from InSAR coherence time series. *Natural Hazards*, *1–9*. https://doi.org/10.1007/s11069-022-05707-y

Campbell, M. K., Bierman, P. R., Schmidt, A. H., Sibello Hernández, R., García-Moya, A., Corbett, L. B., et al. (2022). Cosmogenic nuclide and solute flux data from central Cuban rivers emphasize the importance of both physical and chemical mass loss from tropical landscapes. *Geochronology*, *4*(2), 435–453. https://doi.org/10.5194/gchron-4-435-2022

Crosby, B. T., & Whipple, K. X. (2006). Knickpoint initiation and distribution within fluvial networks: 236 waterfalls in the Waipaoa river, North Island, New Zealand. *Geomorphology*, *82*(1–2), 16–38. https://doi.org/10.1016/j.geomorph.2005.08.023

Demoulin, A. (1998). Testing the tectonic significance of some parameters of longitudinal river profiles: The case of the Ardenne (Belgium, NW Europe). *Geomorphology*, *24*(2–3), 189–208. https://doi.org/10.1016/s0169-555x(98)00016-6

Dewald, A., Heinze, S., Jolie, J., Zilges, A., Dunai, T., Rethemeyer, J., et al. (2013). CologneAMS, a dedicated center for accelerator mass spectrometry in Germany. *Nuclear Instruments and Methods in Physics Research Section B: Beam Interactions with Materials and Atoms*, *294*, 18–23. https://doi.org/10.1016/j.nimb.2012.04.030

DiBiase, R. A., Whipple, K. X., Heimsath, A. M., & Ouimet, W. B. (2010). Landscape form and millennial erosion rates in the San Gabriel Mountains, CA. *Earth and Planetary Science Letters*, *289*(1–2), 134–144. https://doi.org/10.1016/j.epsl.2009.10.036

Diederich, J. L., Wennrich, V., Bao, R., Büttner, C., Bolten, A., Brill, D., et al. (2020). A 68 ka precipitation record from the hyperarid core of the Atacama Desert in northern Chile. *Global and Planetary Change*, *184*, 103054. https://doi.org/10.1016/j.gloplacha.2019.103054

Dunai, T. J. (2010). *Cosmogenic Nuclides: Principles, concepts and applications in the Earth surface sciences*. Cambridge University Press. https://doi.org/10.1017/CBO9780511804519

Dunai, T. J., Lopez, G. A. G., & Juez-Larre, J. (2005). Oligocene-Miocene age of aridity in the Atacama Desert revealed by exposure dating of erosion-sensitive landforms. *Geology*, *33*(4), 321–324. https://doi.org/10.1130/g21184.1

Ericksen, G. E. (1981). *Geology and origin of the Chilean nitrate deposits* (Vol. 37). USGS.

Evenstar, L., Mather, A., Hartley, A., Stuart, F., Sparks, R., & Cooper, F. (2017). Geomorphology on geologic timescales: Evolution of the late Cenozoic Pacific paleosurface in Northern Chile and Southern Peru. *Earth-Science Reviews*, *171*, 1–27. https://doi.org/10.1016/j.earscirev.2017.04.004

Ewing, S. A., Sutter, B., Owen, J., Nishiizumi, K., Sharp, W., Cliff, S. S., et al. (2006). A threshold in soil formation at Earth's arid-hyperarid transition. *Geochimica et Cosmochimica Acta*, *70*(21), 5293–5322. https://doi.org/10.1016/j.gca.2006.08.020

Fang, H., Liu, Y., & Stoesser, T. (2017). Influence of boulder concentration on turbulence and sediment transport in open-channel flow over submerged boulders. *Journal of Geophysical Research: Earth Surface*, *122*(12), 2392–2410. https://doi.org/10.1002/2017jf004221

Farr, T. G., Rosen, P. A., Caro, E., Crippen, R., Duren, R., Hensley, S., et al. (2007). The shuttle radar topography mission. *Reviews of Geophysics*, *45*(2), RG2004. https://doi.org/10.1029/2005rg000183

Garreaud, R. D., Molina, A., & Farias, M. (2010). Andean uplift, ocean cooling and Atacama hyperaridity: A climate modeling perspective. *Earth and Planetary Science Letters*, *292*(1–2), 39–50. https://doi.org/10.1016/j.epsl.2010.01.017

Garreaud, R. D., Vuille, M., Compagnucci, R., & Marengo, J. (2009). Present-day south American climate. *Palaeogeography, Palaeoclimatology, Palaeoecology*, *281*(3–4), 180–195. https://doi.org/10.1016/j.palaeo.2007.10.032

Gerdes, A., & Zeh, A. (2006). Combined U–Pb and Hf isotope LA-(MC-) ICP-MS analyses of detrital zircons: Comparison with SHRIMP and new constraints for the provenance and age of an Armorican metasediment in central Germany. *Earth and Planetary Science Letters*, *249*(1–2), 47–61. https://doi.org/10.1016/j.epsl.2006.06.039

Granger, D. E., Riebe, C. S., Kirchner, J. W., & Finkel, R. C. (2001). Modulation of erosion on steep granitic slopes by boulder armoring, as revealed by cosmogenic ^{26}Al and ^{10}Be. *Earth and Planetary Science Letters*, *186*(2), 269–281. https://doi.org/10.1016/s0012-821x(01)00236-9

Hoffmeister, D. (2018). Meteorological and soil measurements of the permanent weather stations in the Atacama Desert, Chile. In *CRC1211 database*. CRC1211DB.

Houston, J. (2006). Variability of precipitation in the Atacama Desert: Its causes and hydrological impact. *International Journal of Climatology*, *26*(15), 2181–2198. https://doi.org/10.1002/joc.1359

Houston, J., & Hartley, A. J. (2003). The Central Andean west-slope rainshadow and its potential contribution to the origin of hyper-aridity in the Atacama Desert. *International Journal of Climatology*, *23*(12), 1453–1464. https://doi.org/10.1002/joc.938

Jones, R., Small, D., Cahill, N., Bentley, M., & Whitehouse, P. (2019). iceTEA: Tools for plotting and analysing cosmogenic-nuclide surface-exposure data from former ice margins. *Quaternary Geochronology*, *51*, 72–86. https://doi.org/10.1016/j.quageo.2019.01.001

Jordan, T., Riquelme, R., González, G., Herrera, C., Godfrey, L., Colucci, S., et al. (2015). Hydrological and geomorphological consequences of the extreme precipitation event of 24–26 March 2015, Chile. In *XIV Congreso Geologico Chileno (La Serena)*.

Kirchner, J. W., Finkel, R. C., Riebe, C. S., Granger, D. E., Clayton, J. L., King, J. G., & Megahan, W. F. (2001). Mountain erosion over 10 yr, 10 ky, and 10 my time scales. *Geology*, *29*(7), 591–594. https://doi.org/10.1130/0091-7613(2001)029<0591:meoyky>2.0.co;2

Kober, F., Ivy-Ochs, S., Schlunegger, F., Baur, H., Kubik, P. W., & Wieler, R. (2007). Denudation rates and a topography-driven rainfall threshold in northern Chile: Multiple cosmogenic nuclide data and sediment yield budgets. *Geomorphology*, *83*(1–2), 97–120. https://doi.org/10.1016/j.geomorph.2006.06.029

Kohl, C., & Nishiizumi, K. (1992). Chemical isolation of quartz for measurement of in-situ-produced cosmogenic nuclides. *Geochimica et Cosmochimica Acta*, *56*(9), 3583–3587. https://doi.org/10.1016/0016-7037(92)90401-4

Lal, D. (1991). Cosmic ray labeling of erosion surfaces: In situ nuclide production rates and erosion models. *Earth and Planetary Science Letters*, *104*(2–4), 424–439. https://doi.org/10.1016/0012-821x(91)90220-c

Leopold, L. B., & Bull, W. B. (1979). Base level, aggradation, and grade. *Proceedings of the American Philosophical Society*, *123*, 168–202.

Li, Y.-K. (2013). Determining topographic shielding from digital elevation models for cosmogenic nuclide analysis: A GIS approach and field validation. *Journal of Mountain Science*, *10*(3), 355–362. https://doi.org/10.1007/s11629-013-2564-1

Li, Y.-K. (2018). Determining topographic shielding from digital elevation models for cosmogenic nuclide analysis: A GIS model for discrete sample sites. *Journal of Mountain Science*, *15*(5), 939–947. https://doi.org/10.1007/s11629-018-4895-4

Lifton, N., Sato, T., & Dunai, T. J. (2014). Scaling in situ cosmogenic nuclide production rates using analytical approximations to atmospheric cosmic-ray fluxes. *Earth and Planetary Science Letters*, *386*, 149–160. https://doi.org/10.1016/j.epsl.2013.10.052

Lukens, C. E., Riebe, C. S., Sklar, L. S., & Shuster, D. L. (2016). Grain size bias in cosmogenic nuclide studies of stream sediment in steep terrain. *Journal of Geophysical Research: Earth Surface*, *121*(5), 978–999. https://doi.org/10.1002/2016jf003859

Matmon, A., Quade, J., Placzek, C., Fink, D., Arnold, M., Aumaître, G., et al. (2015). Seismic origin of the Atacama Desert boulder fields. *Geomorphology*, *231*, 28–39. https://doi.org/10.1016/j.geomorph.2014.11.008

May, S. M., Hoffmeister, D., Wolf, D., & Bubenzer, O. (2019). Zebra stripes in the Atacama Desert revisited–Granular fingering as a mechanism for zebra stripe formation? *Geomorphology*, *344*, 46–59. https://doi.org/10.1016/j.geomorph.2019.07.014

May, S. M., Meine, L., Hoffmeister, D., Brill, D., Medialdea, A., Wennrich, V., et al. (2020). Origin and timing of past hillslope activity in the hyper-arid core of the Atacama Desert–The formation of fine sediment lobes along the Chuculay Fault System, Northern Chile. *Global and Planetary Change*, *184*, 103057. https://doi.org/10.1016/j.gloplacha.2019.103057

Michalski, G., Bohlke, J. K., & Thiemens, M. (2004). Long term atmospheric deposition as the source of nitrate and other salts in the Atacama Desert, Chile: New evidence from mass-independent oxygen isotopic compositions. *Geochimica et Cosmochimica Acta*, *68*(20), 4023–4038. https://doi.org/10.1016/j.gca.2004.04.009

Mohren, J., Binnie, S. A., Ritter, B., & Dunai, T. J. (2020). Development of a steep erosional gradient over a short distance in the hyperarid core of the Atacama Desert, northern Chile. *Global and Planetary Change*, *184*, 103068. https://doi.org/10.1016/j.gloplacha.2019.103068

Nishiizumi, K. (2004). Preparation of 26 Al AMS standards. *Nuclear Instruments and Methods in Physics Research Section B: Beam Interactions With Materials and Atoms*, *223*, 388–392. https://doi.org/10.1016/j.nimb.2004.04.075

Nishiizumi, K., Caffee, M. W., Finkel, R. C., Brimhall, G., & Mote, G. (2005). Remnants of a fossil alluvial fan landscape of Miocene age in the Atacama Desert of northern Chile using cosmogenic nuclide exposure age dating. *Earth and Planetary Science Letters*, *237*(3–4), 499–507. https://doi.org/10.1016/j.epsl.2005.05.032

Nishiizumi, K., Imamura, M., Caffee, M. W., Southon, J. R., Finkel, R. C., & McAninch, J. (2007). Absolute calibration of Be-10 AMS standards. *Nuclear Instruments and Methods in Physics Research B*, *258*(2), 403–413. https://doi.org/10.1016/j.nimb.2007.01.297

Owen, J. J., Amundson, R., Dietrich, W. E., Nishiizumi, K., Sutter, B., & Chong, G. (2011). The sensitivity of hillslope bedrock erosion to precipitation. *Earth Surface Processes and Landforms*, *36*(1), 117–135. https://doi.org/10.1002/esp.2083

Owen, J. J., Dietrich, W. E., Nishiizumi, K., Chong, G., & Amundson, R. (2013). Zebra stripes in the Atacama Desert: Fossil evidence of overland flow. *Geomorphology*, *182*, 157–172. https://doi.org/10.1016/j.geomorph.2012.11.006

Pfeiffer, M., Morgan, A., Heimsath, A., Jordan, T., Howard, A., & Amundson, R. (2021). Century scale rainfall in the absolute Atacama Desert: Landscape response and implications for past and future rainfall. *Quaternary Science Reviews*, *254*, 106797. https://doi.org/10.1016/j.quascirev.2021.106797

Placzek, C., Granger, D. E., Matmon, A., Quade, J., & Ryb, U. (2014). Geomorphic process rates in the central Atacama Desert, Chile: Insights from cosmogenic nuclides and implications for the onset of hyperaridity. *American Journal of Science*, *314*(10), 1462–1512. https://doi.org/10.2475/10.2014.03

Placzek, C. J., Matmon, A., Granger, D. E., Quade, J., & Niedermann, S. (2020). Evidence for active landscape evolution in the hyperarid Atacama from multiple terrestrial cosmogenic nuclides. *Earth and Planetary Science Letters*, *295*(1–2), 12–20. https://doi.org/10.1016/j.epsl.2010.03.006

Portenga, E. W., & Bierman, P. R. (2011). Understanding Earth's eroding surface with 10 Be.

Quade, J., Reiners, P., Placzek, C., Matmon, A., Pepper, M., Ojha, L., & Murray, K. (2012). Seismicity and the strange rubbing boulders of the Atacama Desert, northern Chile. *Geology*, *40*(9), 851–854. https://doi.org/10.1130/g33162.1

Rech, J. A., Currie, B. S., Jordan, T. E., Riquelme, R., Lehmann, S. B., Kirk-Lawlor, N. E., et al. (2019). Massive middle Miocene gypsic paleosols in the Atacama Desert and the formation of the central Andean rain-shadow. *Earth and Planetary Science Letters*, *506*, 184–194. https://doi.org/10.1016/j.epsl.2018.10.040

Ritter, B., Diederich-Leicher, J. L., Binnie, S. A., Stuart, F. M., Wennrich, V., Bolten, A., & Dunai, T. J. (2022). Impact of $CaSO_4$-rich soil on Miocene surface preservation and Quaternary sinuous to meandering channel forms in the hyperarid Atacama Desert. *Scientific Reports*, *12*, 1–9. https://doi.org/10.1038/s41598-022-22787-9

Ritter, B., Mohren, J., Binnie, S. A., Wennrich, V., Dunkl, I., Albert, R., et al. (2023). Supplementary data - Shaping the Huara intrusive complex in the hyperarid Atacama Desert – Erosional near-stasis contrasting high topographic gradients [Dataset]. CRC1211 Database (CRC1211DB). Retrieved from https://www.crc1211db.uni-koeln.de/search/view.php?doiID=61

Ritter, B., Stuart, F. M., Binnie, S. A., Gerdes, A., Wennrich, V., & Dunai, T. J. (2018). Neogene fluvial landscape evolution in the hyperarid core of the Atacama Desert. *Scientific Reports*, *8*(1), 13952. https://doi.org/10.1038/s41598-018-32339-9

Schween, J. H., Hoffmeister, D., & Löhnert, U. (2020). Filling the observational gap in the Atacama Desert with a new network of climate stations. *Global and Planetary Change*, *184*, 103034. https://doi.org/10.1016/j.gloplacha.2019.103034

Shmilovitz, Y., Morin, E., Rinat, Y., Haviv, I., Carmi, G., Mushkin, A., & Enzel, Y. (2020). Linking frequency of rainstorms, runoff generation and sediment transport across hyperarid talus-pediment slopes. *Earth Surface Processes and Landforms*, *45*(7), 1644–1659. https://doi.org/10.1002/esp.4836

Shobe, C. M., Turowski, J. M., Nativ, R., Glade, R. C., Bennett, G. L., & Dini, B. (2021). The role of infrequently mobile boulders in modulating landscape evolution and geomorphic hazards. *Earth-Science Reviews*, *220*, 103717. https://doi.org/10.1016/j.earscirev.2021.103717

Starke, J., Ehlers, T., & Schaller, M. (2017). Tectonic and climatic controls on the spatial distribution of denudation rates in Northern Chile (18°S to 23°S) determined from cosmogenic nuclides. *Journal of Geophysical Research: Earth Surface*, *122*(10), 1949–1971. https://doi.org/10.1002/2016jf004153

Stone, J., Fifield, K., Beer, J., Vonmoos, M., Obrist, C., Grajcar, M., et al. (2004). Co-precipitated silver–metal oxide aggregates for accelerator mass spectrometry of ^{10}Be and ^{26}Al. *Nuclear Instruments and Methods in Physics Research Section B: Beam Interactions with Materials and Atoms*, *223*, 272–277. https://doi.org/10.1016/s0168-583x(04)00580-4

Strahler, A. N. (1957). Quantitative analysis of watershed geomorphology. *Eos, Transactions American Geophysical Union*, *38*(6), 913–920. https://doi.org/10.1029/tr038i006p00913

Struck, M., Jansen, J. D., Fujioka, T., Codilean, A. T., Fink, D., Egholm, D. L., et al. (2018). Soil production and transport on postorogenic desert hillslopes quantified with ^{10}Be and ^{26}Al. *GSA Bulletin*, *130*(5–6), 1017–1040. https://doi.org/10.1130/b31767.1

Vásquez, P., & Sepúlveda, F. (2013). *Cartas Iquique y Pozo Almonte - Región de Tarapacá No. 161-163 Escala 1:100.000*. Carta Geológica de Chile Serie Geología Básica.

Vicencio Veloso, J. (2022). Analysis of an extreme precipitation event in the Atacama Desert in January 2020 and its relationship to humidity advection along the Southeast Pacific. *Atmósfera*, *35*, 421–448.

von Blanckenburg, F. (2005). The control mechanisms of erosion and weathering at basin scale from cosmogenic nuclides in river sediment. *Earth and Planetary Science Letters*, *237*(3–4), 462–479. https://doi.org/10.1016/j.epsl.2005.06.030

Wang, F., Michalski, G., Seo, J.-H., Granger, D. E., Lifton, N., & Caffee, M. (2015). Beryllium-10 concentrations in the hyper-arid soils in the Atacama Desert, Chile: Implications for arid soil formation rates and El Niño driven changes in Pliocene precipitation. *Geochimica et Cosmochimica Acta*, *160*, 227–242. https://doi.org/10.1016/j.gca.2015.03.008

Wittmann, H., & von Blanckenburg, F. (2009). Cosmogenic nuclide budgeting of floodplain sediment transfer. *Geomorphology*, *109*(3–4), 246–256. https://doi.org/10.1016/j.geomorph.2009.03.006

Wolff, R., Hetzel, R., Dunkl, I., & Anczkiewicz, A. A. (2021). New constraints on the exhumation history of the western Tauern Window (European Alps) from thermochronology, thermokinematic modeling, and topographic analysis. *International Journal of Earth Sciences*, *110*(8), 2955–2977. https://doi.org/10.1007/s00531-021-02094-w

Yager, E., Kirchner, J., & Dietrich, W. (2007). Calculating bed load transport in steep boulder bed channels. *Water Resources Research*, *43*(7), W07418. https://doi.org/10.1029/2006wr005432

References From the Supporting Information

Bürgmann, R. (2014). Warning signs of the Iquique earthquake. *Nature*, *512*(7514), 258–259. https://doi.org/10.1038/nature13655

Farley, K. A., Wolf, R. A., & Silver, L. T. (1996). The effects of long alpha-stopping distances on (U-Th)/He ages. *Geochimica et Cosmochimica Acta*, *60*(21), 4223–4229. https://doi.org/10.1016/s0016-7037(96)00193-7

Gerdes, A., & Zeh, A. (2009). Zircon formation versus zircon alteration—New insights from combined U–Pb and Lu–Hf in-situ LA-ICP-MS analyses, and consequences for the interpretation of Archean zircon from the central zone of the Limpopo belt. *Chemical Geology*, *261*(3–4), 230–243. https://doi.org/10.1016/j.chemgeo.2008.03.005

Jackson, S. E., Pearson, N. J., Griffin, W. L., & Belousova, E. A. (2004). The application of laser ablation-inductively coupled plasma-mass spectrometry to in situ U–Pb zircon geochronology. *Chemical Geology*, *211*(1–2), 47–69. https://doi.org/10.1016/j.chemgeo.2004.06.017

Sager, C., Airo, A., Arens, F. L., Rabethge, C., & Schulze-Makuch, D. (2020). New types of boulder accumulations in the hyper-arid Atacama Desert. *Geomorphology*, *350*, 106897. https://doi.org/10.1016/j.geomorph.2019.106897

Santos, M., Lana, C., Scholz, R., Buick, I., Schmitz, M., Kamo, S., et al. (2017). A new appraisal of Sri Lankan BB Zircon as a reference material for LA-ICP-MS U-Pb Geochronology and Lu-Hf Isotope Tracing. *Geostandards and Geoanalytical Research*, *41*(3), 335–358. https://doi.org/10.1111/ggr.12167

Schärer, U. (1984). The effect of initial ^{230}Th disequilibrium on young UPb ages: The Makalu case, Himalaya. *Earth and Planetary Science Letters*, *67*(2), 191–204. https://doi.org/10.1016/0012-821x(84)90114-6

Stacey, J. T., & Kramers, J. (1975). Approximation of terrestrial lead isotope evolution by a two-stage model. *Earth and Planetary Science Letters*, *26*(2), 207–221. https://doi.org/10.1016/0012-821x(75)90088-6

Wiedenbeck, M., Alle, P., Corfu, F., Griffin, W. L., Meier, M., Oberli, F. V., et al. (1995). Three natural zircon standards for U-Th-Pb, Lu-Hf, trace element and REE analyses. *Geostandards Newsletter*, *19*, 1–23. https://doi.org/10.1111/j.1751-908x.1995.tb00147.x

Erratum

The originally published version of this article contained several typographical errors. In Figure 6, ^{10}Be in the X-axis in parts A and B were incorrect. In the X-axis, the description should be ^{10}Be [years]. In Table 1, the ratios under the Norm. ^{26}Al/^{10}Be column were incorrect. In addition, the supporting information has been updated with a revised Table S1. These errors have been corrected, and this may be considered the authoritative version of record.